

## DETECTION OF BULK MOTIONS IN THE ICM OF THE CENTAURUS CLUSTER

RENATO A. DUPKE & JOEL N. BREGMAN  
 University of Michigan, Ann Arbor, MI 48109-1090  
*Draft version April 26, 2024*

## ABSTRACT

Several recent numerical simulations of off-center cluster mergers predict that significant angular momentum with associated velocities of a few  $\times 10^3$  km s<sup>-1</sup> can be imparted to the resulting cluster. Such gas bulk velocities can be detected by the Doppler shift of X-ray spectral lines with *ASCA* spectrometers. Using two *ASCA* observations of the Centaurus cluster (Abell 3526), we produced a velocity map for the gas in the cluster's central regions. We also detected radial and azimuthal gradients in temperature and metal abundance distributions, which seem to be associated with the infalling sub-group centered at NGC 4709 (Cen 45). More importantly, we found a significant (>99.8% confidence level) velocity gradient along a line near-perpendicular to the direction of the incoming sub-group and with a maximum velocity difference of  $\sim 3.4 \pm 1.1 \times 10^3$  km s<sup>-1</sup>. It is unlikely ( $P < 0.002$ ) that the observed velocity gradient is generated by gain fluctuations across the detectors. While the observed azimuthal temperature and abundance variations can be attributed to the interaction with Cen 45, we argue that the intracluster gas velocity gradient is more likely due to a previous off-center merging event in the main body of the Centaurus cluster.

*Subject headings:* galaxies: clusters: individual (Abell 3526) — intergalactic medium — cooling flows  
 — X-rays: galaxies —

ApJ in press

## 1. INTRODUCTION

Most of the visible mass in clusters is in the form of a very hot ( $T \sim 10^7$ – $10^8$  K) diffuse X-ray emitting plasma enriched with heavy elements that permeates the cluster, the so-called intracluster medium (ICM). Galaxy clusters are believed to be formed by the infall/merging of smaller scale systems (bottom-up hierarchical scenario). The merging of sub-clumps induces several long lasting intracluster gas signatures that can be observed in the X-ray range, such as temperature and density inhomogeneities, destruction of cooling flows and metal abundance gradients and generation of gas bulk velocities. Spatial distributions of surface brightness and gas temperature can be directly compared to numerical hydrodynamical+N body simulations of cluster mergers to provide a picture of the evolutionary stage of clusters (e.g. Evrard 1990; Katz & White 1993; Roettiger, Burns & Loken 1993,1996; Schindler & Muller 1993; Pearce, Thomas & Couchman 1994; Navarro, Frenk & White 1995; Evrard, Metzler, & Navarro 1996; Roettiger, Loken & Burns 1997, Ricker 1998; Takizawa & Mineshige 1998; Burns et al. 1999; Takizawa 1999, 2000 and references therein).

*ASCA* observations have shown significant gas temperature variations in many clusters, which are often attributed to recent mergers and this suggests that galaxy clusters are still forming. However, when determining the precise evolutionary stage of the intracluster gas, the distribution of gas temperature and surface brightness alone have limitations. This is because they represent only a 2-D projection of a 3-D system. In order to reduce degeneracies and to determine the cluster evolution stage more precisely it is extremely important to obtain as much information as possible about the dynamics of the intracluster gas.

Several recent numerical simulations of off-center cluster mergers predict that significant angular momentum can be imparted to the resulting cluster with velocities approaching a few thousand km s<sup>-1</sup>. Simulations also show that gas bulk flows may last for several Gyr after the merger (e.g. Roettiger, Loken & Burns 1997, Ricker 1998; Roettiger, Stone, & Mushotzky 1998; Takizawa & Mineshige 1998; Burns et al. 1999; Takizawa 1999, 2000; Roettiger & Flores 2000). Therefore, measurements of radial velocity distribution of the intracluster gas provides a very important additional source of information that, coupled with temperature and surface brightness distributions, can be directly compared to numerical simulations to determine the evolutionary stage of galaxy clusters.

Radial velocity measurements of the intracluster gas can be obtained from X-ray observations, but require accurate determinations of spectral line centroids. The precision with which a line centroid can be measured is a function of the square root of the number of line photons, the FWHM of the instrument, the line energy and, in practice, it strongly depends on knowledge of the instrumental gain (conversion between pulse height and energy). The instruments on-board *ASCA* have the capability of measuring directly such ICM bulk velocities. Furthermore, *ASCA*'s spectrometer's gain calibration is already well-understood as to allow reliable velocity measurements.

Recently, using the GISs on-board *ASCA*, we have detected a velocity gradient in the intracluster gas of the Perseus cluster. The spectral analysis of 8 different *ASCA* pointings encompassing a region of  $\sim 1 h_{50}^{-1}$  Mpc radius around the center of the Perseus cluster (Dupke & Bregman 2000, 2001), showed a significant velocity gradient of  $\geq 1000$  km s<sup>-1</sup>Mpc<sup>-1</sup> at the 90% confidence. How-

ever, the GISs have worse energy resolution than the SISs, which severely limited the ability to precisely constraint the velocity gradient amplitude. Ideally, one would like to use the higher energy resolution of the SISs to measure ICM bulk velocities.

The Centaurus cluster provides us with an excellent opportunity to measure intracluster gas velocities more precisely. It is a bright, nearby cluster, with high metal abundances (well isolated spectral lines) and shows signs of interaction with an infalling subgroup (Cen 45) located  $\sim 13\text{--}18'$  from the center, which is associated with the galaxy NGC 4709. Furthermore, it has been an *ASCA* target for a long exposure ( $\sim 90$  ksec) taken in 1-CCD mode with the best calibrated CCDs. These observational characteristics make Centaurus an optimal target for gas velocity measurements.

In this paper we analyze the central regions of Centaurus and determine the velocity structure of this system using data from two different *ASCA* pointings. In sections 2 & 3 we describe the general characteristics of the Centaurus cluster, of the *ASCA* pointings analyzed and of data reduction procedures. In section 4 we investigate whether the velocity differences between Cen 30 and 45 previously observed optically by other authors can be corroborated by X-ray velocity analysis using the GISs. In section 5 we present the spectral fitting results of SIS data for the observation with the longest exposure (taken in 1995) and estimate the effects of gain variations in our results as a function of frequency and position. In section 6 we show the results of the spectral analysis of another *ASCA* pointing taken 2 years earlier, with a shorter exposure. In section 7 we briefly discuss the nature of the small and large scale bulk motions detected in Centaurus.

## 2. THE CENTAURUS CLUSTER

Centaurus (Abell 3526) is classified as Bautz-Morgan type I, it has an optical redshift of 0.0104 and is one of the closest X-ray bright clusters of galaxies. It has a small cooling flow and the estimated accretion mass rate is  $< 30\text{--}50$  solar masses per year (e.g. Matilsky, Jones & Forman 1985; Allen & Fabian 1994; White, Jones & Forman 1997; Peres et al. 1998). Its X-ray emission is relatively smooth, slightly elliptical in shape and is strongly peaked on the cD galaxy NGC4696. The average temperature of the gas in the cluster is  $\sim 3.5$  keV (e.g. Mitchell & Mushotzky 1980; Matilsky et al. 1985; Thomas, Fabian & Nulsen 1987; Edge & Steward 1991). *ASCA* GIS & SIS analyses of the central region of Centaurus have shown evidence of a strong central metal abundance enhancement (Allen & Fabian 1994; Fukazawa et al. 1994) varying from supersolar in the very central regions down to 0.3 solar at  $\sim 13'$  ( $1'$  at Centaurus distance is equivalent to  $\sim 19 h_{50}^{-1}$  kpc). Furthermore, the region where metal abundances are enhanced is dominated by SN Ia ejecta (Allen et al. 2000) indicating the presence of a radial “chemical gradient”.

Early studies of galaxy velocities in the Centaurus cluster have shown the existence of bimodality in velocity space (Lucey, Currie & Dickens 1986a,b). Two galaxy groups are clearly separated: The main group (Cen 30) which is centered on the cD galaxy (NGC 4696) shows an average radial velocity of  $\sim 3000$  km s $^{-1}$  and a veloc-

ity dispersion of  $\sim 590$  km s $^{-1}$ . The second group (Cen 45) is associated with the galaxy NGC 4709 at  $\gtrsim 15'$  from NGC 4696. It has an average radial velocity of  $\sim 4600$  km s $^{-1}$  and a velocity dispersion of  $\sim 280$  km s $^{-1}$ . Lucey et al. (1986a,b) concluded that the Cen 45 and Cen 30 are at the same distances and that Cen 45 is being accreted by the Centaurus cluster, based on a detailed analysis of the color-magnitude, luminosity function and galaxy radius distribution. Improved redshift measurements of the central regions of Centaurus confirmed the galaxy velocity bimodal distribution: the “true” cluster Cen 30 having an average velocity of  $3397 \pm 139$  km s $^{-1}$  and a velocity dispersion of  $933 \pm 118$  km s $^{-1}$ , and Cen 45 having an average velocity of  $4746 \pm 43$  km s $^{-1}$  and a velocity dispersion of  $131 \pm 43$  km s $^{-1}$  (Stein et al. 1997).

The X-ray surface brightness contours of Centaurus are slightly elliptical and NGC 4709 is located near the major axis (Allen & Fabian 1994), suggesting that the elongation towards Cen 45 can be associated with the elongation of the gravitational well along the collision axis. More recently, Churazov et al. (1999) has derived an X-ray temperature map of the Centaurus cluster using the *ASCA* satellite and found a region where the intracluster gas is significantly hotter ( $\gtrsim 5$  keV) than the surroundings ( $\sim 3.5\text{--}4.0$  keV). The region with higher gas temperature is apparently associated with Cen 45 and indicates the presence of shocks due to the infall of subcluster Cen45.

## 3. DATA REDUCTION & ANALYSIS

*ASCA* carries four large-area X-ray telescopes, each with its own detector: two Gas Imaging Spectrometers (GIS) and two Solid-State Imaging Spectrometers (SIS). Each GIS has a  $50'$  diameter circular field of view and covers a energy range of 0.8–10 keV, while each SIS has a  $22'$  square field of view and covers an energy range of 0.4–10 keV. For all pointings analyzed in this work we selected data taken with high and medium bit rates, with cosmic ray rigidity values  $\geq 6$  GeV/c, with elevation angles from the bright Earth of  $\geq 20^\circ$ , and from the Earth’s limb of  $\geq 5^\circ$  (GIS) or  $\geq 10^\circ$  (SIS); we also excluded times when the satellite was affected by the South Atlantic Anomaly. Rise time rejection of particle events was performed on GIS data and hot and flickering pixels were removed from SIS data. We estimated the background from blank sky files provided by the *ASCA* Guest Observer Facility. In the spectral fittings we used XSPEC v10.0 software (Arnaud 1996) to fit the GIS & SIS spectra separately and simultaneously. The spectra were fitted using the *mekal* and *Vmekal* thermal emission models, which are based on the emissivity calculations of Mewe & Kaastra (Mewe, Gronenschild & van den Oord 1985; Mewe, Lemen & van den Oord 1986; Kaastra 1992), with Fe L calculations by Liedahl et al. (1995). Abundances are measured relative to the solar photospheric values (Anders & Grevesse 1989), in which Fe/H= $4.68 \times 10^{-5}$  by number. Galactic photoelectric absorption was incorporated using the *wabs* model (Morrison & McCammon 1983); Throughout the paper the hydrogen column density is assumed to be fixed to the Galactic value, i.e.,  $8.07 \times 10^{20}$  cm $^{-2}$  (Dickey & Lockman 1990 - W3nH tool<sup>1</sup>), unless stated otherwise. Spectral channels were grouped to have at least 25 counts/channel. Since 1994, there have

<sup>1</sup> <http://heasarc.gsfc.nasa.gov/cgi-bin/Tools/w3nh/w3nh.pl>

been increasing discrepancies between SIS and GIS in the low energy end of the spectra, due to a decrease in X-ray efficiency in the SISs<sup>2</sup>; Therefore, energy ranges for both instruments were restricted to 0.8–10 keV, in all spectral fittings.

The central regions of the Centaurus cluster were observed by *ASCA* in June of 1993 (P93) and on July of 1995 (P95) for  $\sim 24$  ksec and 87 ksec, respectively; the characteristics of these two pointings are shown in Table 1. The original energy resolution of the spectrometers on-board *ASCA* were 8% and 2% at 5.9 keV for GISs and SISs, respectively. The SISs energy resolution has been steadily degrading with time (e.g. Dotani et al. 1997) due to the increases in dark current and decline in X-ray signal charge transfer efficiency (Rasmussen et al. 1998). For the best pointing analyzed in this work (P95) the energy resolution is  $\sim 2.9\%$  and  $3.1\%$  at 6.0 keV for SIS 0 & 1, respectively. Furthermore, for P95 the SIS observations were taken in 1-CCD mode using the best calibrated chips of each spectrometer (S0C1 and S1C3).

Since there is a mild cooling flow at the center of Centaurus we added a cooling flow component (Mushotzky & Szymkowiak 1988) to the `mekal` thermal emission model in the central region, to compare the temperature of the hot component in the central region with that of the outer regions. We tied the maximum temperature of the cooling flow to the temperature of the thermal component, and we fixed the minimum temperature at 0.1 keV. The abundances of the two spectral components (`mekal` and `cflow`) were tied together. We also applied a single (but variable) absorption to both spectral components.

We have noticed an unusual gain variation in the SISs when comparing spectral fittings including the FeK complex to those excluding it. It is probably due to the assumption that the charge transfer inefficiency is independent of X-ray energy during the initial gain standard correction procedure (see below). Typically, spectral fittings that excluded the FeK line complex showed higher best-fit redshift values. Since we are looking for relative velocity measurements this effect should not affect our analysis. However, we also show the results from spectral fittings excluding the FeK complex, where the energy range considered goes from 0.8-6.0 keV and are denoted by a sub-index FeL.

For P95 we noticed significant discrepancies of best-fit redshifts for some regions (e.g. P8) between SIS 0 & 1 spectral fits. This is probably due to different spatial distribution of gain fluctuations in different chips. Therefore, we avoided performing simultaneous spectral fittings using these two spectrometers. The statistics are sufficiently good that radial velocity distributions can be measured precisely on each instrument separately. For P93 however, the statistics are not good enough to notice significant changes of the best-fit parameters when spectra from SIS 0 & 1 are fitted separately. Therefore, for that pointing, we show only the results of joint spectral fittings.

For the analysis of the cluster's central regions with the SISs we selected a set of 9 different extraction regions within  $8'$  of the cluster's center using the SISs. The very central region included the cluster core (P0), and the other regions were distributed symmetrically around P0, cen-

tered  $5'$  away and with a radius of  $3'$ . These regions are illustrated in Figure 1, where they are overlaid on the X-ray surface brightness contours. This set of extraction regions was applied to both pointings (P95 & P93). We applied a correction for the position angles between these pointings ( $19.6^\circ$ ), so that each extraction region corresponded to the same position in the sky for both observations.

Since P93 was taken in 4-CCD mode and the bulk of the cluster emission was extended over 2 CCDs in both SIS 0 & 1, we have taken into account the overall interchip gain differences when comparing spectra from different CCDs (see below). In doing so, if an extraction region crossed over 2 CCDs we considered only the fraction of that region that included the largest number of counts in one CCD. This procedure minimizes the errors involved in the process of gain correction. Therefore, when comparing the results from pointings P93 to P95 one should notice that the centroids of the extraction regions may be slightly ( $< 1'$ ) shifted with respect to one another for P93 regions: P1 (shifted towards P2), P4 (shifted towards P3), P5 (shifted towards P6) and P8 (shifted towards P7).

For the GIS analysis of the outer ( $>8'$ ) parts of Centaurus, we selected two sets of extraction regions: in the first set, the region encompassing Cen 45 (circle centered  $11'$  from NGC 4696 towards Cen 45 with a  $8'$  radius) was compared to the average. The second set of regions was chosen analogously to that for the SIS analysis of the central  $8'$  and it included a central region ( $0-5'$ ) and 8 large regions symmetrically distributed around the center, at a distance of  $12'$  from the center and with a radius of  $5'$ . Since the GISs have a poorer energy resolution than the SISs, we joined the 8 outer regions by adjacent pairs (1-2, 3-4, 5-6, 7-8) in order to improve photon statistics. These regions are also illustrated in Figure 1. The objective of the analysis of the outer regions was to check for corroboration in X-ray frequencies of the velocity difference seen in the optical analyses between Cen 45 and Cen 30.

#### 4. GIS GLOBAL VELOCITY MEASUREMENTS OF CEN 45

As we mentioned previously, the galaxy velocity distribution in Centaurus is bimodal (Lucey, Currie & Dickens 1986a,b). One of the velocity components is associated with the main body of the cluster (Cen30) and has a radial systemic velocity of  $\sim 3000$  km s<sup>-1</sup> and another component associated with the galaxy NGC 4709  $\sim 15'$  away from Cen 30 has a radial systemic velocity of  $\sim 4500$  km s<sup>-1</sup> and is generally denoted by Cen 45. We examined whether the optical velocity differences have an X-ray counterpart. We applied a similar technique that was used in the analysis of velocity measurements in the Perseus cluster with the GISs on-board *ASCA* (see Dupke & Bregman 2001 for details).

The most obvious spatial configuration to test for velocity differences between the region associated with Cen45 and Cen 30 is to extract spectra from a circular region large enough to encompass the bulk of Cen 45 ( $11'$  away from the center with a  $8'$  radius – denoted C45) and compare the best-fit redshift values to the average (total field-of-view minus C45). The best-fit parameters of the spectral fittings of the C45 region and of the average region are shown in Table 2. C45 region is significantly hotter

<sup>2</sup> [heasarc.gsfc.nasa.gov/docs/asca/watchout.html](http://heasarc.gsfc.nasa.gov/docs/asca/watchout.html), also Hwang et al. 1999

( $T=5.47\pm 0.27$  keV) than the average gas temperature of Centaurus ( $3.44\pm 0.03$  keV), and has a lower metal abundance ( $0.5\pm 0.09$  Solar) than the average ( $0.77\pm 0.03$  Solar), consistent with a central negative radial abundance gradient. The best-fit redshift value for C45 is found to be  $3.27^{+1.58}_{-1.13} \times 10^{-2}$ , which is significantly ( $>90\%$  confidence limits) higher than the average redshift of the rest of the cluster  $1.81^{+0.05}_{-0.01} \times 10^{-2}$ .

The errors cited above are spectral fitting errors and do not include any uncertainties related to gain variations across the detectors. In order to estimate the latter we used a similar procedure to that used previously in the GIS velocity analysis of Perseus (Dupke & Bregman 2001). We used the GIS gain map determined from the Cu-K line at 8.048 keV (Idesawa et al. 1995) to estimate the velocity differences expected purely from residual gain variations across the detector. We compared the average gain values of the C45 region for each instrument with that of the field-of-view excluding C45. The gain variations across each detector are corrected in-house with the ftool ASCALIN V.9.0t. If we assume that there are still significant gain fluctuations across the detector and, conservatively, that these fluctuations are on the same order as those of the pre-processed data then the expected difference between the two regions due purely to gain variations is  $\sim 1870$  km s $^{-1}$  (C45 having the higher radial velocity). Therefore, the “real” velocity difference (not directly associated with gain variations) is  $\sim 2.6\pm 2.0 \times 10^3$  km s $^{-1}$  ( $1-\sigma$  errors), which is consistent with the optical velocity measurements of  $\sim 1500$  km s $^{-1}$ .

The gain scatter across the C45 region in GIS 2 & 3 is relatively high (on the same order of the velocities that we are trying to measure) lowering the significance of the observed velocity differences. Therefore, we looked for another spatial extraction configuration that minimized the gain fluctuations inside the extraction regions but still encompassing Cen 45 and with enough photon statistics to measure velocities correspondent to the optical measurements. The resulting configuration chosen is also shown in Figure 1 and it consists of 4 regions symmetrically distributed around the central region (circle centered on the X-ray peak with a  $5'$  radius). The four regions are pairs of adjacent circular regions ( $12'$  away with  $5'$  radius). They are labeled as J12, J34, J56 & J78. This configuration shows a reduction of intrachip gain scatter by  $\sim 17\%$  for GIS 2 and  $\sim 32\%$  for GIS 3 with respect to the previous configuration. The high temperature region detected by Churazov et al. (1999) associated with Cen 45 is located mostly within J56. The best-fitting parameter values for this configuration are also shown in Table 2. It can be seen that the only region which shows significantly different redshifts ( $>90\%$  confidence) with respect to the central region is J56 and the corresponding velocity difference is  $\sim 1.77\pm 0.96 \times 10^3$  km s $^{-1}$  ( $1-\sigma$  errors).

The results above are consistent with the optical measurements and indicate that significant velocity gradients in clusters can be detected even with the GISs, which have worse energy resolution than the SISs on-board ASCA. In the next sections we use the SISs to analyze the very central regions of the Centaurus cluster. Besides having a better energy resolution (by a factor of  $\gtrsim 2.5$ ), the SIS spatial gain fluctuations are more stable than that of the

GIS. Therefore, radial velocities can be measured with a substantially higher precision.

## 5. SIS ANALYSIS OF THE CENTRAL REGIONS OF CENTAURUS

### 5.1. SIS Observation of July 1995 (P95)

P95 is the best pointing analyzed in this work and probably one of the best pointings in the ASCA archive for the analysis of gas bulk motions. The combination of long-exposure (Table 1), clock mode (1-CCD), and cluster’s center positioning in the CCDs (roughly at the center of S0C1 and S1C3) makes this pointing near-optimal for velocity studies with ASCA. The best-fit values for temperature, abundance and redshift obtained from spectral fittings of the central regions are shown in Table 3 and plotted in Figures 2a,b as a function of the position angle for SIS 0 & 1, respectively. The indicated errors in Figures 2a,b are  $90\%$  confidence limits.

It can be seen from Figures 2a,b that the temperature distribution is consistent with the presence of a cooling flow (with a best fit mass deposition rate  $\lesssim 10$  solar masses per year). The best-fit temperatures are found to be typically slightly higher using SIS 1 data than those obtained with SIS 0. The temperature in the center is  $\sim 2.68\pm 0.05$  keV and shows a positive gradient outwards up to a maximum value of  $\sim 3.59\pm 0.09$  keV and  $\sim 3.85\pm 0.12$  keV for SIS 0 & 1, respectively. The  $90\%$  confidence limits for the best-fit values in the central region are indicated by the two horizontal lines in Figures 2a,b. Furthermore, the observed temperature gradient is not purely radial. One can notice a significant azimuthal temperature gradient, which is roughly symmetric and with a maximum towards the direction of Cen 45, which is the region in between the two vertical lines in all plots. The azimuthal temperature distribution has only one axis of symmetry and, therefore, is not consistent with the “cross” pattern shape of ASCA PSF scattering.

The metal abundance distribution is consistent with the existence of a central abundance gradient (Figure 2a,b and Table 3). In general, if different elemental metal abundances were tied such as to produce solar abundance ratios the fits were significantly worse (often with  $\chi^2_\nu \approx 1.3$ ). There was a significant improvement in the spectral fittings when individual metal abundances were let free to vary ( $\chi^2_\nu \approx 1$ ), resulting in strongly non-solar abundance ratios. This is consistent with the observed dominance of SN Ia ejecta in the central regions of this cluster (Allen et al. 2000). Furthermore, letting the individual elemental abundances free to vary did not cause significant changes in the best-fit values of temperature, Fe abundance or redshifts. Therefore, we report here only the spectral fittings for an absorbed (Galactic) *vmekal* (abundances free to vary) spectral model (with an extra cooling flow component for the central region). The metal abundance within the inner  $3'$  was found to be  $1.13\pm 0.05$  solar and  $1.23\pm 0.06$  solar, for the SIS 0 & 1, respectively. The  $90\%$  confidence limits for the abundance in the central region are shown by the horizontal lines in Figures 2a,b. One can see also indications of an azimuthal metal abundance gradient. In the outer  $5'$  the metal abundance drops significantly towards the direction of Cen 45 (P3, P4, P5, P6 & P7 for SIS 0 and P4, P5 & P7 for SIS 1). The minimum metal

abundance values were reached around pointings P4 & P5 in both detectors, where the best-fit value is  $\sim 0.86 \pm 0.1$  solar.

The azimuthal distributions of redshifts are shown in Figures 2a,b (bottom plot) as a function of the position angle. The original SIS 0 best-fit redshift values were too close to 0 so that full determination of 90% confidence errors was compromised in XSPEC. Therefore, all redshifts in that chip were boosted up by a slope correction of  $0.9\%^3$ . This redshift-boosting does not affect our results since we are not interested in the absolute redshift values, but only in the redshift differences between regions. SIS 1 redshifts are displayed directly (without any gain boosting).

From Figure 2a we can see that the SIS 0 data shows a very significant velocity gradient. Regions P3 & P4 have significantly lower velocities than regions P6, P7 & P8 by  $\sim 2.67 \pm 0.21 \times 10^3 \text{ km s}^{-1}$  for SIS 0 and  $2.73 \pm 0.27 \times 10^3 \text{ km s}^{-1}$  for SIS 1 ( $1\text{-}\sigma$  errors). Both velocity-discrepant sets of regions have significantly different velocities (on the order of  $\sim 1350 \text{ km s}^{-1}$  at  $> 90\%$  confidence level) with respect to the clusters center. Although the velocity gradient is also seen in SIS 1 data, its significance is lower than that obtained using SIS 0 data. This is due to the significantly smaller effective number of counts of SIS 1 with respect to SIS 0 (30% less counts) and to the larger gain spatial variability of SIS 1. Figure 2b shows the azimuthal distribution of best-fit redshifts obtained using SIS 1 data. It can be seen that for the ‘‘low velocity’’ regions (P3 & P4) the redshifts are significantly different from that of the central region and also from most of the regions in the ‘‘high velocity’’ hemisphere (P6 & P8). There is one region (P8) for which analysis of SIS 0 & 1 spectra gives discrepant results. Although the distribution of radial velocities determined using SIS 1 are less constrained than that determined using SIS 0, the overall azimuthal distributions of velocities are consistent with one another. *The velocity gradient found with SIS 1 is maximum along the same direction (P4–P6) as that determined from SIS 0 and has the same magnitude ( $\sim 380 \text{ km s}^{-1} \text{ arcmin}^{-1}$ ).* The velocity differences are unlikely caused by spectral modeling effects since regions with discrepant velocities have similar temperatures and metal abundances.

To assess the significance of the velocity differences described in the previous paragraph, we chose two regions where we consistently found the maximum velocity differences, P4 and P6, and we applied the F-test. We simultaneously fitted spectra from SIS 0 & 1 for each of the two regions and analyzed  $\chi^2$  variations associated to the change in the number of degrees of freedom. We compared the  $\chi^2$  of fits which assumed the redshifts to be the same in the two projected spatial regions P4 & P6, i.e.,  $z_{S0P4} = z_{S1P4} = z_{S0P6} = z_{S1P6}$ , to that of fits which allowed the redshifts in the two regions to vary independently, reducing the number of degrees of freedom by one. For the latter we tied the redshifts within each of the two regions together, i.e.,  $(z_{S0P4} = z_{S1P4}) \neq (z_{S0P6} = z_{S1P6})$ , where  $z_{SiPj}$  is the redshift of region  $j$  with instrument

SIS  $i$ . This is justified by the lack of significant changes in the best-fit redshifts obtained by different instruments for the same region. The difference between the  $\chi^2$  of these two fits must follow a  $\chi^2$  distribution with one degree of freedom (e.g. Bevington 1969). The value  $F(n) = \frac{\chi^2(n-1) - \chi^2(n)}{\chi^2(n)}$ , where  $n$  is the number of fitting terms, is related to the probability that the additional term significantly contributes to the reduction of the  $\chi^2$  statistic. Comparison of the  $F(n)$  from the fits with locked and unlocked redshifts to tabulated values of  $F$  indicates that the best-fit redshifts obtained for P4 & P6 are discrepant at  $> 99.99\%$  level. We show in Figure 3 the 90% and 99% confidence contours for two interesting parameters (redshifts) of regions P4 and P6 as well as the line correspondent to equal redshifts.

## 5.2. SIS Gain Variations & Redshift Dependence on Gain

The SIS performance has gradually degraded due to the accumulated energetic particle radiation damage, which is manifested by an increase in residual dark-current distribution (RDD) and in signal charge transfer inefficiency (CTI). Although the RDD effect is negligible in 1-CCD mode (Dotani 2000<sup>4</sup>) the increase of the CTI reduces the apparent X-ray energy and thus causes a systematic variation of gain with time (Dotani et al.<sup>5</sup>, Rasmussen et al.<sup>6</sup>). This effect is different for different chips resulting in enhancements of interchip global gain variations.

Correction for the above mentioned effect have been carried out using the Ni background fluorescence line originated from the kovar (iron-nickel-cobalt alloy), which covers the frame store region of the chips and also using observations of Cas A. To investigate the time dependence of the average CTI, the center energy of the Ni line has been recorded every 3 months from standard chips (S0C1 and S1C3) in 1 CCD mode (Dotani et al.<sup>7</sup>). The decrease of the line energy is well approximated by a linear function of time. Furthermore, the gain variation with time was observed to vary non-uniformly for different spectral lines after CTI correction. This may be a consequence of the assumption that the CTI is independent of X-ray energy as well as from scatter of the line energies among the pointing positions.

The event files analyzed in this work were corrected by the tool ASCALIN V0.9t, using the most recent gain calibration file `sisph2pi_110397.fits`. The line center energies are different from chip to chip by at most 2% (interchip gain variation). Since we are showing results for SIS 0 & 1 separately, we do not worry about global gain variation differences between these detectors. However, we need to estimate the gain variation across each CCD (intrachip gain variation). We did so by analyzing the gain scatter across the detectors measured using Cas A data. After the standard correction analysis is completed, the systematic errors on the FeK $\alpha$  line centers are reduced to  $\sim 0.29\%$  (870km/s) for S0C1 and  $\sim 0.28\%$  (840 km/s) for S1C3.

<sup>3</sup> where the new line energy is related to the old energy in the standard way, i.e.,  $E_{new} = \frac{E_{old}}{\text{slope}} - \text{intercept}$

<sup>4</sup> [www.astro.isas.ac.jp/~dotani/rdd.html](http://www.astro.isas.ac.jp/~dotani/rdd.html)

<sup>5</sup> [heasarc.gsfc.nasa.gov/docs/asca/newsletters/sis\\_calibration5.html](http://heasarc.gsfc.nasa.gov/docs/asca/newsletters/sis_calibration5.html)

<sup>6</sup> [heasarc.gsfc.nasa.gov/docs/asca/newsletters/sis\\_performance2.html](http://heasarc.gsfc.nasa.gov/docs/asca/newsletters/sis_performance2.html)

<sup>7</sup> [heasarc.gsfc.nasa.gov/docs/asca/newsletters/sis\\_calibration5.html](http://heasarc.gsfc.nasa.gov/docs/asca/newsletters/sis_calibration5.html)

The values mentioned above are based on a more recent preliminary calibration analysis performed by Dotani and kindly provided to us by K. Mukai<sup>8</sup>. Using the older calibration references cited in the previous paragraphs<sup>9</sup> would give a  $\sigma_{gain}$  of 0.22% and 0.38% for SIS 0 & SIS 1, respectively. This discrepancy does not change any of the results obtained in this paper. However, the larger observed uncertainties associated with the determination of best-fit redshifts in SIS 1 suggests that  $\sigma_{gain}$  for SIS 1 should be greater than that for SIS0.

We tested the sensitivity of our observations to possible residual gain variations across the SISs using Monte Carlo simulations. Supposing the redshift to be constant for the two regions where we find maximum velocity differences (P4 & P6), we generated fake spectra for both spectrometers and compared the best-fit redshift differences. Then we calculated the probability to find the same redshift differences (or greater than) that we observed in the real regions, for SIS 0 & 1. The procedure used is completely analogous to that used in testing the effects of residual gain variations across the GISs in the velocity measurements for the Perseus cluster (Dupke & Bregman 2000, 2001) and we refer the reader to that paper for details.

We simulated 1000 SIS 0 & 1 spectra corresponding to the real observation using the same spectral model, parameters and responses correspondent to the real regions. The simulated spectra were then grouped, fitted and had a gain uncertainty added to their best-fit redshift values. We assumed that the gain variations follow a Gaussian distribution with a standard deviation ( $\sigma_{gain}$ ), which is different for each spectrometer, and a zero mean. We adopted as our  $1-\sigma$  gain variations ( $\sigma_{gain}$ ) for the SIS 0 & 1 the values described above, i.e., 0.29% and 0.28%, respectively. We then calculated the probability of finding the same (or greater) redshift differences between the two simulated regions that we found in the real ones, i.e.,  $\Delta z = 0.009$ ; that probability is found to be  $\lesssim 0.002$ .

In Figure 4 we plot the dependence of the chance probability (described in the previous paragraph) on the assumed  $\sigma_{gain}$  of the spectrometers (for the purpose of illustration  $\sigma_{gain}$  for SIS 0 is assumed to be the same as that for SIS 1, which roughly represents the real case). In Figure 5 we also indicate the value for  $\sigma_{gain}$  estimated in the previous paragraphs ( $\sim 0.28\%$ ). In our real case we observed not only two but at least three regions (more than three if SIS 0 data alone is considered) with discrepant redshifts (P3, P4 & P6). Therefore, the significance of the velocity gradient found in Centaurus obtained by the method described above (99.8%) should be taken as a lower limit.

### 5.3. Spectral Fittings Without the FeK Line Complex

The velocity measurements presented in the previous section were derived from spectral fittings of SIS 0 & 1 encompassing the usable energy range of the spectrometers, i.e., from 0.8 to 10 keV, and are mainly driven by the FeK $_{\alpha}$  line complex. Since the Centaurus cluster has very high ( $\sim$ solar) metal abundances it allows for the possibility of reliably measuring velocities using other spectral lines, or at least, excluding the FeK line complex energy range. When we fitted the spectra from SIS 0 & 1 for different

energy ranges we noticed a systematic gain discrepancy between spectral fittings that included FeK line complex from those excluding it. Excluding energies corresponding to both FeK and FeL complexes in the spectral fittings produced best-fit velocities (determined from spectral lines of other individual elements) that were more consistent with those fits that included the FeL line complex than with those that included the FeK line complex. When the FeK lines were included the measured redshifts were consistently lower. As mentioned previously, this effect is most likely due to the assumption that the CTI is independent of X-ray energy during the in-house calibration process.

In order to check how the observed velocity distributions were affected by the effect mentioned in the previous paragraph we performed a series of redshift measurements excluding the FeK region ( $< 6$  keV). The spectral fitting characteristics were completely analogous to that used in the last section. The resulting best-fit values for temperature, metal abundance and radial velocities are listed in Table 4 and the redshift distributions for SIS 0 & 1 are shown in Figures 5a,b. The best-fit temperatures found when the FeK line complex is excluded from the analysis are, in general, slightly higher than, but similar to, those obtained using the full useable energy range. The azimuthal temperature gradient is still marginally seen. The measured temperatures in the center are  $2.84 \pm 0.03$  keV (SIS0) &  $2.77^{+0.03}_{-0.07}$  keV (SIS1), rising to  $3.70 \pm 0.12$  keV (SIS0) &  $4.11 \pm 0.16$  keV (SIS0) towards the direction of Cen 45. The abundance measurements are not well constrained enough to detect a central metal enhancement and are consistent with a flat profile ( $\sim 1.25 \pm 0.25$  Solar) with a large dispersion.

It can be seen from Figures 5a,b that, although the best-fit redshifts are typically higher than those in Figures 2a,b, the behavior of the azimuthal distributions with and without the FeK complex energy range are very similar. A significant ( $> 90\%$  confidence) velocity gradient is also found. The velocity distribution reaches a minimum around regions P3 & P4 and a maximum at region P6 & P7. The velocity gradient is found to be steeper for SIS 0. The corresponding maximum velocity differences are  $\sim 6.3 \pm 1.2 \times 10^3$  km s $^{-1}$  for SIS 0 and  $\sim 3.18 \pm 0.96 \times 10^3$  km s $^{-1}$  for SIS 1 ( $1-\sigma$  errors).

### 5.4. SIS Observation of June 1993 (P93)

In the previous sections we have shown that the velocity gradient in the ICM of the Centaurus cluster is detected with high significance using SIS 0 & 1 data including and excluding the FeK line complex. We have also shown that it is not due to gain variations within the CCDs. Since ASCA has observed the Centaurus cluster several times, we can test the reliability of the velocity measurements by performing the same analysis for another pointing, with different observing characteristics (e.g. observing date, CCD clock mode, position on the CCD, etc). Out of the two archived pointings in the ASCA archive that cover the whole central regions of Centaurus, we chose the one with larger spatial coverage and exposure time. We refer to this pointing as P93 and list its characteristics in Table 1.

<sup>8</sup> see [www.astro.lsa.umich.edu/~rdupke/dotani.ps](http://www.astro.lsa.umich.edu/~rdupke/dotani.ps)

<sup>9</sup> [heasarc.gsfc.nasa.gov/docs/asca/newsletters/rad\\_dam\\_sis3.html](http://heasarc.gsfc.nasa.gov/docs/asca/newsletters/rad_dam_sis3.html)

P93, however, has three main disadvantages when compared with P95. Firstly, it has been taken in 4-CCD mode. The energy resolution of the SISs in 2-4 CCD modes has degraded by a factor of four with time with respect to 1-CCD mode observations due to the increase of RDD<sup>10</sup>. RDD effects were already not negligible for 4-CCD mode observations at the time P93 was taken<sup>11</sup> (Rasmussen et al. 1994). Secondly, the effective exposure time is relatively short, around four times smaller than for P95; Thirdly, the cluster's central regions are mainly extended over two chips in each spectrometer (S0C1 & S0C2 and S1C3 & S1C0). These two chips have different overall gain off-sets, requiring a more elaborated correction for gain variations, thus increasing the uncertainties of the measured redshifts. The first two of the above mentioned problems cause, effectively, larger statistical uncertainties when determining velocities. The last problem is more serious. If not taken into account, interchip gain difference can be much larger than the velocities one is trying to measure, thus being able to artificially create, erase, or amplify velocity gradients.

We corrected for interchip gain variations as follows: since the cluster's center is located very near the separation between chips, we selected a region with  $3'$  radius centered on the X-ray peak and analyzed the spectra of the two parts of that region that fell on each separate chip;  $3'$  at Centaurus distance corresponds to  $\sim 57 h_{50}^{-1}$  kpc. At that distance from the cluster center we assume that any velocity gradient that we measure between the two semi-regions is purely due to interchip gain variations. If there were true velocity differences detectable by the spectrometers in that region ( $\gtrsim 600 \text{ km s}^{-1}$ ) the gas would be gravitationally unbound. By comparing the velocity difference between these two regions we found the correction factors that should be applied to each CCD so that the gain difference between chips did not affect the velocity measurements. To join data from both spectrometers (to improve statistics) we corrected for the global gain differences for each pair of chips in each spectrometer. In order to bring all redshift values from all four chips to a unique solution within the central region we determined the gain correction factors that should be applied simultaneously to S0C1, S0C2, S1C3 & S1C0 as 1.0%, 1.2%, 0.6% & 1.0%, respectively.

After applying the gain correction described above we selected extraction regions analogous to those used for P95, i.e. with  $3'$  radius at  $5'$  from the center with a  $\sim 20^\circ$  rotation to compensate for the roll angle difference between the two pointings. If one of these regions crossed the chip boundaries and therefore could be separated in two parts we ignored the part that had the smaller number of counts (the improvement in photon statistics does not justify the uncertainties generated by the gain correction procedures).<sup>12</sup>

The results are shown in Figure 6 and listed in Table 5. The temperature and abundance distributions are consistent with, though less significant than, those obtained

for P95. The azimuthal temperature gradient outside the cooling flow region is clearly seen. The maximum temperature is reached towards the Cen 45 group ( $T=3.49\pm 0.25$  keV), the temperature within the central  $3'$  is  $2.54^{+0.07}_{-0.04}$  keV and the central abundance gradient is marginally visible. The large errors associated with velocity measurements in P93 are due to: 1) the effective exposure being  $\sim 4$  times smaller than in P95; 2) the observations being taken in 4-CCD mode, which worsens the energy resolution ( $\gtrsim 3.5\%$  at 6.0 keV); 3) the correcting procedure for interchip gain variations involves assumptions that may be oversimplified (e.g. the non-existence of true gas velocity differences within a  $3'$  radius. Nevertheless, *a velocity gradient is also seen roughly in the same orientation as that detected in P95!* In particular, P3 & P4 have significantly ( $> 68\%$  confidence) lower redshifts than P6. The velocity difference correspondent to regions P4 & P6 is  $\Delta V \sim (1.8 \pm 1.5) \times 10^3 \text{ km s}^{-1}$  ( $1-\sigma$  errors), consistent with the velocity measurements from P95.

## 6. DISCUSSION

Spatially resolved spectral analysis of ASCA SIS 0 & 1 data carried out in this work strongly indicates the presence of significant azimuthal temperature, metal abundance and velocity gradients in the ICM of the Centaurus cluster. The temperature and metal abundance profiles derived in this work indicate the presence of a very mild cooling flow and a central abundance enhancement, consistent with those found in previous works. Both temperature and abundance gradients are steeper (with different signs) towards the Southeast direction, where Cen 45 is located. The increase in temperature and mild dilution of metal abundances towards Cen 45 is consistent with the hypothesis that Cen 45 is in the process of merging with the main body of the Centaurus cluster (Cen 30).

The velocity distribution shows a significant gradient along a direction roughly *perpendicular* to the direction of Cen 45 subgroup. The amplitude of the velocity gradient (along the P4-P6 direction) can be as high as  $\sim 25 h_{50} \text{ km s}^{-1} \text{ kpc}^{-1}$ . The velocity gradient is significantly ( $> 90\%$  confidence) detected with both SISs on-board ASCA. The velocity gradient is also seen in a different ASCA observation performed  $\sim 2$  years earlier, although with smaller significance. We have shown in the previous sections that the velocity gradient is not caused by gain fluctuations across the SIS chips, thus suggesting the presence of large-scale bulk motions of the intracluster gas in this cluster.

A tentative global velocity distribution for the central regions of the Centaurus cluster that summarizes the results obtained in this paper is plotted in Figure 7 and listed in Table 6. The data points show a weighted average velocity departure from the median  $\Delta V$  for all cases that we have analyzed previously, i.e., SIS 0 & 1 for P95, SIS 0 & 1 for P95 without the FeK line complex and SIS 0 & 1 for P93. The errors include the fitting errors and a constant gain uncertainty corresponding to the  $1-\sigma$  intrachip gain

<sup>10</sup> [heasarc.gsfc.nasa.gov/docs/asca/newsletters/sis\\_calibration5.html](http://heasarc.gsfc.nasa.gov/docs/asca/newsletters/sis_calibration5.html)

<sup>11</sup> [heasarc.gsfc.nasa.gov/docs/asca/newsletters/sis\\_performance2.html](http://heasarc.gsfc.nasa.gov/docs/asca/newsletters/sis_performance2.html)

<sup>12</sup> Within the extraction regions considered in the analysis of the central regions (circles of  $3'$  radius  $5'$  from the center) some photons fell in the top two chips (in detector coordinates) of each spectrometer (S0C0 & S0C3 and S1C2 & S1C1). However, these regions are small and the gain correction procedure described above would create much higher uncertainties than what we would gain statistically by including those regions. Therefore, we consider photons detected only within the two chips described in the previous paragraph.

fluctuation described in the previous sections, i.e., 0.28%. The direction towards Cen 45 is shown by the vertical lines and the uncertainties of the velocity measurements for the very central regions is indicated by the horizontal lines. For illustration, we fit a simple solid body rotation function to the data and obtain a best-fit maximum rotational velocity of  $1.59 \pm 0.32 \times 10^3 \text{ km s}^{-1}$ .<sup>13</sup>

Similarly to the case of the Perseus cluster, the large scale X-ray elongation is near perpendicular to the direction where the velocity gradient is maximum. However, in the case of Centaurus, the elongation towards Cen 45 can be directly associated with the elongation of the gravitational well along the collision axis. At smaller scales ( $\lesssim 10'$ ) there is evidence for isophotal twisting (Mohr, Fabricant & Geller 1993) and the major axis of the surface brightness elongation shifts  $\sim 50^\circ$  towards the direction of maximum gas velocity gradient.

One way of generating such large angular momentum in clusters is through cluster-cluster mergers. Several recent numerical simulations of off-center cluster mergers predict residual intracluster gas bulk rotation with velocities of a few thousand  $\text{km s}^{-1}$  (Ricker 1998; Roettiger, Stone, & Mushotzky 1998; Takizawa 1999, 2000; Roettiger & Flores 2000) indicating that a high fraction of the merging energy can be transferred to gas rotation (Pearce, Thomas, & Couchman, 1994). In the case of Centaurus there is growing evidence indicating that this cluster is in the process of merging with the galaxy group Cen 45 including: (1) the galaxy radial velocity bimodality detected by Lucey et al. (1986a,b), (2) the large scale gas radial velocity bimodality shown in this work (GIS analysis); (3) the large scale temperature gradient detected towards NGC 4709, which is expected from heating due to interaction between the two subgroups (Churazov et al. 1999); (4) the small scale azimuthal temperature and abundance gradients detected towards Cen 45 (this work); (5) the morphological segregation both in velocity and physical space: Cen 30 is dominated by early type galaxies and Cen 45 by late types (Stein, Jerjen & Federspiel 1997);

Simulations of head-on mergers show that the core of the primary cluster changes from being spherical before core-crossing to an elongated shape along the merger direction after core-crossing (Gomez 2000). This is not observed in the core of Cen 30 (the X-ray elongation in the core is actually near perpendicular to the collision axis). In a head-on collision with a smaller mass sub-unit, the core of the main cluster may display cooler regions towards the side opposite to the strongest bow shock (at the boundary of the two systems) shortly (0.25 Gyr) after core crossing (e.g. Gomez 2000). This would be consistent with the smooth azimuthal temperature gradient along the direction towards Cen 45 (P1, P0, P5). However, this scenario, i.e., we are in a post-core crossing epoch, faces several difficulties. Firstly, this is a very short period of time in order to establish full rotation. Secondly, even if rotation is not fully established significant gas bulk motions are seen only after the boundary shock has encompassed the cores of

the two sub-systems (Ricker 1998), and thirdly, galaxies in the two sub-systems in Centaurus are still in a clearly segregated state.

Even though it has been suggested that mergers erase cooling flows (e.g. Edge, Steward & Fabian 1992, Roettiger et al. 1993) and central abundance gradients, recent simulations of cooling-flow-cluster mergers show that, even in head-on mergers, the bow shock that appears in between the colliding systems can protect the gas from mixing and cooling flows can survive mergers depending on the produced ram-pressure of the gas in the infalling cluster (Gomez et al. 2000, see also Fabian & Daines 1991). Cooling flow survival in mergers is predicted to be even more probable in *off-center* mergers (Gomez et al. 2000). Further, large scale merger-induced gas rotation can last for a few crossing times (Roettiger & Flores 2000), which suggests a more likely scenario to explain the gas velocity distribution in Centaurus, that is, the velocity gradient in Centaurus pre-existed the current merger and is not connected to the recent infall of Cen 45. In this scenario the observed velocity gradient was generated by some previous off-center merger, that happened  $> 0.2\text{-}0.6 h_{50}^{-1} \text{ Gyr}$  (circulation time) ago and did not destroy either the cooling flow or the central abundance gradient<sup>14</sup>. This past merger event could have been a reasonably isolated event, in which case the temperature asymmetry in the maps of Churazov et al. (1999) could actually be due to the effects of a current head-on collision with a previously rotating cluster. If this is the case, Centaurus may provide a crucial observational basis for future comparison to (currently unavailable) numerical simulations of cluster mergers where the components have a previously imparted intrinsic angular momentum.

However, the velocity structure observed could be also created by a past series of matter accretion events from filamentary structures, in the intersection of which clusters are believed to form. The poor spatial resolution of the spectrometers on-board ASCA does not allow us to construct a detailed velocity map that would discriminate between a more or less systematic ICM “rotation” from a more chaotic ICM “stormy weather” as predicted by Burns et al. 1999. Multiple off-center long exposure velocity measurements of intracluster gas with the *Chandra* and *XMM-Newton* satellites will allow us to reduce the systematic uncertainties related to gain variations, and consequently, to determine ICM velocities in the central and outer regions more precisely. This, combined with more specific cluster-cluster merger simulations will allow us to strongly constrain the current evolutionary stage of the Centaurus cluster.

## 7. SUMMARY

We have used, for the first time, spatially resolved spectroscopy for determination of ICM radial-velocities in the Centaurus cluster. The main results of our velocity analysis are:

1. The gas velocity distribution at  $> 8'$  determined

<sup>13</sup> It should be noted that bulk velocities as high as these can be, in principle, measured also through high resolution differential measurements of the Sunyaev-Zel'dovich effect across the line of maximum velocity difference, especially in cool clusters such as Centaurus, where the thermal component is weakly dominant below 300 GHz and  $(\frac{\Delta T}{T})_{CMBR} \sim 10^{-4} - 10^{-3}$ .

<sup>14</sup> After this paper was submitted we learned that an extensive gas temperature analysis of multiple pointings of the Centaurus cluster by Furusho et al. (2001) also supports this scenario.



with the GISs shows that the region associated with Cen 45 has a radial velocity higher than that of the rest of the cluster by  $\sim 1.77 \pm 0.96 \times 10^3 \text{ km s}^{-1}$ . This is consistent with the optically determined velocity differences between Cen 45 and Cen 30 of  $\sim 1.35 \pm 0.19 \times 10^3 \text{ km s}^{-1}$  (Stein et al. 1997).

2. We found azimuthal temperature and abundance gradients in the cluster's central regions ( $< 8'$ ). The azimuthal temperature variations are in agreement with the temperature maps determined previously by other authors (Churazov et al. 1999). Both temperature and metal abundance variations seem to be directly related to the infall of the Cen 45 subgroup.
3. The gas velocity distribution at  $< 8'$  determined with the SISs reveals a significant velocity gradient ( $>99.9\%$  confidence) along a direction near-perpendicular to the direction towards Cen45. This detection is found to be significant in both SIS 0 & 1 separately and also in another ASCA pointing taken two years earlier. The velocity gradient does not show any clear correlation with

the temperature or metal abundance gradients. It is not due to spectral modeling effects or to intrachip gain fluctuations. The velocity gradient is consistent with gas bulk rotation with circular velocity  $1.59 \pm 0.32 \times 10^3 \text{ km s}^{-1}$ , implying that gas kinetic energy is comparable to the thermal energy in the intracluster gas of Centaurus.

4. Comparison to cluster-merger numerical simulations, available in the literature, suggests that the velocity gradients that we detected in the central regions of Centaurus are not associated with the current infall of the Cen 45 subgroup. Therefore, we believe that it is more likely that the central velocity gradient is remnant of one or more previous off-center merger events.

We would like to thank J. Irwin for the many helpful discussions and suggestions and the anonymous referee for useful suggestions. We particularly thank K. Mukai for providing information about ASCA SIS gain calibrations that was crucial to this work. We acknowledge support from NASA Grant NAG 5-3247. This research made use of the HEASARC ASCA database and NED.

#### REFERENCES

- Allen, S. W., & Fabian, A. C. 1994, *MNRAS*, 269, 409  
 Allen, S. W., Fabian, A. C., Johnstone, R. M., Arnaud, K. A., & Nulsen, P. E. J. 2000, *MNRAS* in press (astro-ph/9910188)  
 Anders, E., & Grevesse N. 1989, *Geochimica et Cosmochimica Acta*, 53, 197  
 Arnaud, K. A. 1996, in *Astronomical Data Analysis Software and Systems V*, ASP Conf. Series volume 101, eds. Jacoby, G., & Barnes, J., p.17  
 Bevington, P. R. 1969, *Data Reduction and Error Analysis for the Physical Sciences* (New York: McGraw-Hill), p.200  
 Burns, J. O., Loken, C., Roettiger, K., Rizza, E., Bryan, G., Norman, M. L., Gomez, P. and Owen, F. N. 1999, "Life Cycles of Radio Galaxies", ed. J. Biretta et al., *New Astronomy Reviews*, astro-ph/9908361  
 Churazov, E., Gilfanov, M., Forman, W., & Jones, C. 1999, *ApJ*, 520, 105  
 Dickey, J. M., & Lockman, F. J. 1990, *ARA&A*28, 215  
 Dotani, T., Yamashita, A., Ezuka, H., Takahashi, K., Crew, G., Mukai, K., & the SIS team 1997, *ASCA News* 5, April. (see also [heasarc.gsfc.nasa.gov/docs/asca/gis\\_sis\\_effective\\_area.html](http://heasarc.gsfc.nasa.gov/docs/asca/gis_sis_effective_area.html))  
 Dupke, R. A., & Bregman, J. N. 2001, *ApJ*, 547, 705  
 Dupke, R. A., & Bregman, J. N. 2000, in proceedings of the IAP2000 meeting "Constructing the Universe with Clusters of Galaxies", eds. F. Durret, D. Gerbal (astro-ph/0011100).  
 Edge, A. C., Stewart, G. C., & Fabian, A. C. 1992, *MNRAS*, 258, 177  
 Edge, A. C., & Stewart, G. C. 1991, *MNRAS*, 252, 414  
 Evrard, A. E. 1990, *ApJ*, 363, 349;  
 Evrard, A. E., Metzler, C. A., & Navarro, J. F. 1996, *ApJ*, 469, 494;  
 Fabian, A. C. & Daines, S. J. 1991, *MNRAS*, 252, 17  
 Fukazawa, Y., Ohashi, T., Fabian, A. C., Canizares, C. R., Ikebe, Y., Makishima, K., Mushotzky, R. F., & Yamashita, K. 1994, *PASJ*, 46, 55  
 Furusho, T., Yamasaki, N.Y., Ohashi, T., Shibata, R., Kagei, T., Ishisaki, Y., Kikuchi, K., Ezawa, H. & Ikebe 2001, *PASJ astro-ph/0103358*  
 Gomez, P. L., Loken, C., Roettiger, K., & Burns, J. O. 2000, *ApJ*, in press (astro-ph/0009465)  
 Hwang, U., Mushotzky, R. F., Burns, J. O., Fukazawa, Y., & White, R. A. 1999, *ApJ*, 516, 604  
 Idesawa, E., Asai, K., Ishisaki, Y., Kubo, H., Kubota, A., Makishima, K., Tamura, T., Tashiro, M., & the GIS team 1995, [heasarc.gsfc.nasa.gov/docs/asca/gain.html](http://heasarc.gsfc.nasa.gov/docs/asca/gain.html)  
 Kaastra, J. S. 1992, *An X-Ray Spectral Code for Optically Thin Plasmas*, (Internal SRON-Leiden Report, updated version 2.0)  
 Katz, N., & White, S. D. M. 1993, *ApJ*, 412, 455;  
 Liedahl, D. A., Osterheld, A. L., & Goldstein, W. H. 1995, *ApJ*, 438, L115  
 Lucey, J. R., Currie, M. J., & Dickens, R. J. 1986a, *MNRAS*, 221, 453  
 Lucey, J. R., Currie, M. J., & Dickens, R. J. 1986b, *MNRAS*, 222, 427  
 Matilsky, T., Jones, C., & Forman, W. 1985, *ApJ*, 291, 621  
 Mewe, R., Gronenschild, E. H. B. M., & Van den Oord, G. H. J. 1985, *A&AS*, 62, 197  
 Mewe, R., Lemen, J. R., & Van den Oord, G. H. J. 1986, *A&AS*, 65, 511  
 Mitchell, R. J., & Mushotzky, R. F., 1980, *ApJ*, 236, 730  
 Mohr, J. J., Fabricant, D. G., & Geller, M. J. 1993, *ApJ*, 413, 492  
 Morrison, R., & McCammon, D. 1983, *ApJ*, 270, 119  
 Mushotzky, R. F., & Szymkowiak, A. E. 1988, in *Cooling Flows in Clusters and Galaxies*, ed. A. C. Fabian (Dordrecht: Kluwer), 53  
 Navarro, J. F., Frenk, C. S., & White, S. D. M. 1995 *MNRAS*, 275, 720  
 Pearce, F. R., Thomas, P. A., & Couchman, H. M. P. 1994, *MNRAS*, 268,953;  
 Peres, C. B., Fabian, A. C., Edge, S. W., Johnstone, R. M., & White, D. A. 1998, *MNRAS*, 298, 416  
 Rasmussen, A., Crew, G., Ricker, G. & the SIS Team, 1994, *ASCANEWS* 2.  
 Ricker, P. M. 1998, *ApJ*, 496, 670  
 Roettiger, K., Burns, J. O., & Loken, C. 1993, *ApJ*, 407, 53;  
 Roettiger, K., Burns, J. O., & Loken, C. 1996, *ApJ*, 473, 651  
 Roettiger, K., Loken, C., & Burns, J. O. 1997, *ApJS*, 109, 307  
 Roettiger, K., Stone, J. M. & Mushotzky, R. 1998, *ApJ*, 1493, 62  
 Roettiger, K. & Flores, R. 2000, *ApJ*, 538, 92  
 Schindler, S., & Muller, E. 1993, *A&A*, 272, 137 ;  
 Stein, P., Jerjen, H., & Federspiel, M. 1997, *A&A*, 327, 952  
 Takizawa, M., & Mineshige, S. 1998, *ApJ*, 499, 82;  
 Takizawa, M. 1999, *ApJ*, 520,514  
 Takizawa, M. 2000, *ApJ*, in press (astro-ph/9910441)  
 Thomas, P. A, Fabian, A. C., & Nulsen, P. E. J. 1987, *MNRAS*, 228, 973

DRAFT VERSION APRIL 26, 2024

Preprint typeset using L<sup>A</sup>T<sub>E</sub>X style emulateapj v. 14/09/00

## FIGURE CAPTIONS

FIG. 1.— Distribution of the spatial regions for the pointings analyzed in this work. Regions labeled with a  $P_i$ , where  $i=0-8$ , denote the set of extraction regions used in the SIS 0 & 1 analysis of the central regions for P95 and P93. The radius of each circular region is  $3'$  and they are  $5'$  away from the cluster's center. The larger regions denoted J12, J34, J56 and J78 are combinations two-by-two of circular regions  $12'$  away with  $5'$  radius used for the GIS velocity analysis of the outer regions of Centaurus. For the same analysis a circular region  $11'$  away with  $8'$  radius was also selected and is denoted by C45. The approximate position of NGC 4709 is towards the bottom left of C45. Surface brightness contours of Centaurus are overlaid.

FIG. 2.— a)Azimuthal distribution of temperature (TOP), metal abundance (MIDDLE), and redshift (BOTTOM) as a function of the position angle (radians) obtained from the analysis of SIS 0 data for P95. The first data point from the left for all plots corresponds to P1, increasing to P8 (last). For all plots dark solid horizontal lines represent the 90% confidence limits for the central region (P0). The region between vertical lines indicates the approximate direction of Cen 45. Errors for all plots are 90% confidence. A velocity difference equivalent to  $2700 \text{ km s}^{-1}$  is also indicated by horizontal dashed lines. b)Same as (a) but for SIS 1

FIG. 3.— Confidence contour plot for two interesting parameters (redshifts) for regions P4 & P6 using SIS 0 & 1 data for P95. The two contours correspond to 90% and 99% confidence levels. The line of equal redshifts is also indicated. The contours are found from simultaneous spectral fittings of four data groups (P4 SIS 0&1 and P6 SIS 0&1). The redshifts parameters for both instruments are tied together for the spectral fittings of the same region.

FIG. 4.— Probability of finding redshift differences equal or greater than what we observed for the real data (P4×P6) by chance as a function of the standard deviation of intrachip gain variations for the SISs. The  $\sigma_{gain}$  for SIS 0 is assumed to be the same as that for SIS 1 in this plot for illustration purposes. The actual value of  $\sigma_{gain}$  used in this paper ( $\sim 0.28\%$ ) is also indicated.

FIG. 5.— a)Azimuthal distribution of redshifts as a function of the position angle (radians) obtained from the spectral fittings of SIS 0 data for P95 when the FeK line complex energy range was excluded. First data point from the left for all plots corresponds to P1, increasing to P8 (last). For all plots dark solid horizontal lines represent the 90% confidence limits for the central region (P0). The region between vertical lines indicate the approximate direction of Cen 45. Errors for all plots are 90% confidence. A velocity difference equivalent to  $6300 \text{ km s}^{-1}$  is also indicated by horizontal dashed lines. b)Same as (a) but for SIS 1 and the horizontal dashed lines indicated a velocity difference equivalent to  $4300 \text{ km s}^{-1}$ .

FIG. 6.— Azimuthal distribution of Temperature (TOP), Metal Abundance (MIDDLE), and Redshift (BOTTOM) as a function of the position angle (radians) obtained from the simultaneous spectral fittings of SIS 0 & 1 data for P93. The first data point from the left for all plots corresponds to P1, increasing to P8 (last). The errorbars indicated show 90% confidence errors for temperature and abundances and  $68\%(1\sigma)$  for redshifts. The dark solid horizontal lines represent the confidence limits for the central region (P0). The region between vertical lines indicate the approximate direction of Cen 45. A velocity difference equivalent to  $1800 \text{ km s}^{-1}$  is also indicated by horizontal dashed lines.

FIG. 7.— Average azimuthal gas radial velocity distribution for the central regions of the Centaurus cluster. Data points indicate the weighted average of the departure from the median. The errors also include a  $1\sigma$  gain variation of  $0.28\%$  (typical for the SIS chips at 1995) for all cases (all instruments, all pointings) analyzed in this work. The first data point from the left for all plots corresponds to P1, increasing to P8 (last). The dark solid horizontal lines represent the 68% confidence limits for the central region (P0). The region between the two vertical lines indicates the approximate direction of Cen 45. The solid line indicate the bestfit for a simple solid-body cosine function with a corresponding maximum rotational velocity of  $\sim 1600 \pm 300 \text{ km s}^{-1}$ .

TABLE 1  
X-RAY OBSERVATIONS

Pointing	Sequence Number	Date Observed	RA (2000)	DEC (2000)	GIS EXP <sup>a</sup> (ksec)	SIS EXP <sup>b</sup> (ksec)
P95	83026000	1995-07-19	12h48m21.60s	-41°19'44.8''	56.4	67.9
P93	80032000	1993-06-30	12h48m24.00s	-41°17'16.4''	14.7	16.6

<sup>a</sup>Effective Exposure (Average for GIS 2 & 3)

<sup>b</sup>Effective Exposure (Average for SIS 0 & 1)

TABLE 2  
GIS SPECTRAL FITTINGS FOR P95<sup>a,b</sup>

Region	Temperature <sup>c</sup> (keV)	Abund (Solar)	Redshift (10 <sup>-2</sup> )	$\chi^2_\nu$
C45	5.47 <sup>+0.28</sup> <sub>-0.27</sub>	0.50 <sup>+0.09</sup> <sub>-0.09</sub>	3.27 <sup>+1.58</sup> <sub>-1.13</sub>	1.062
All-C45	3.44 <sup>+0.03</sup> <sub>-0.03</sub>	0.77 <sup>+0.03</sup> <sub>-0.03</sub>	1.81 <sup>+0.05</sup> <sub>-0.01</sub>	1.206
J0	2.73 <sup>+0.02</sup> <sub>-0.02</sub>	1.09 <sup>+0.05</sup> <sub>-0.05</sub>	1.81 <sup>+0.05</sup> <sub>-0.01</sub>	1.102
J12	3.67 <sup>+0.09</sup> <sub>-0.08</sub>	0.54 <sup>+0.07</sup> <sub>-0.06</sub>	2.35 <sup>+0.37</sup> <sub>-0.52</sub>	0.983
J34	4.16 <sup>+0.13</sup> <sub>-0.13</sub>	0.47 <sup>+0.08</sup> <sub>-0.08</sub>	1.93 <sup>+1.07</sup> <sub>-0.08</sub>	0.969
J56	4.67 <sup>+0.17</sup> <sub>-0.17</sub>	0.44 <sup>+0.09</sup> <sub>-0.08</sub>	2.40 <sup>+0.60</sup> <sub>-0.50</sub>	0.969
J78	3.83 <sup>+0.10</sup> <sub>-0.09</sub>	0.42 <sup>+0.06</sup> <sub>-0.06</sub>	1.61 <sup>+0.26</sup> <sub>-0.65</sub>	0.970

<sup>a</sup>Errors are 90% confidence

<sup>b</sup>0.8–10.0 keV

<sup>c</sup> $N_H$  fixed at the Galactic value

TABLE 3  
SPECTRAL FITTINGS FOR P95<sup>a,b,c</sup>

Region	T(SIS0) <sup>d,e</sup> (keV)	T(SIS1) <sup>d</sup> (keV)	Abund (SIS0) (Solar)	Abund (SIS1) (Solar)	z (SIS0) (10 <sup>-2</sup> )	z (SIS1) (10 <sup>-2</sup> )
P0	2.67 <sup>+0.03</sup> <sub>-0.03</sub>	2.69 <sup>+0.06</sup> <sub>-0.05</sub>	1.13 <sup>+0.06</sup> <sub>-0.03</sub>	1.23 <sup>+0.07</sup> <sub>-0.06</sub>	1.32 <sup>+0.02</sup> <sub>-0.01</sub>	1.41 <sup>+0.04</sup> <sub>-0.02</sub>
P1	2.94 <sup>+0.06</sup> <sub>-0.06</sub>	2.74 <sup>+0.08</sup> <sub>-0.06</sub>	1.11 <sup>+0.12</sup> <sub>-0.10</sub>	1.10 <sup>+0.15</sup> <sub>-0.12</sub>	1.33 <sup>+0.15</sup> <sub>-0.10</sub>	1.58 <sup>+0.38</sup> <sub>-0.23</sub>
P2	3.11 <sup>+0.07</sup> <sub>-0.06</sub>	3.02 <sup>+0.07</sup> <sub>-0.07</sub>	0.96 <sup>+0.09</sup> <sub>-0.09</sub>	1.11 <sup>+0.12</sup> <sub>-0.11</sub>	1.33 <sup>+0.16</sup> <sub>-0.11</sub>	1.40 <sup>+0.08</sup> <sub>-0.05</sub>
P3	3.43 <sup>+0.09</sup> <sub>-0.08</sub>	3.54 <sup>+0.09</sup> <sub>-0.05</sub>	0.83 <sup>+0.08</sup> <sub>-0.08</sub>	1.04 <sup>+0.11</sup> <sub>-0.10</sub>	0.88 <sup>+0.15</sup> <sub>-0.05</sub>	0.88 <sup>+0.15</sup> <sub>-0.05</sub>
P4	3.59 <sup>+0.08</sup> <sub>-0.09</sub>	3.84 <sup>+0.11</sup> <sub>-0.12</sub>	0.89 <sup>+0.09</sup> <sub>-0.08</sub>	0.84 <sup>+0.11</sup> <sub>-0.10</sub>	0.88 <sup>+0.19</sup> <sub>-0.05</sub>	0.85 <sup>+0.34</sup> <sub>-0.12</sub>
P5	3.56 <sup>+0.10</sup> <sub>-0.09</sub>	3.86 <sup>+0.13</sup> <sub>-0.12</sub>	0.83 <sup>+0.09</sup> <sub>-0.10</sub>	0.87 <sup>+0.13</sup> <sub>-0.12</sub>	1.33 <sup>+0.12</sup> <sub>-0.09</sub>	1.33 <sup>+0.16</sup> <sub>-0.51</sub>
P6	3.36 <sup>+0.09</sup> <sub>-0.09</sub>	3.37 <sup>+0.11</sup> <sub>-0.11</sub>	0.86 <sup>+0.10</sup> <sub>-0.09</sub>	0.99 <sup>+0.14</sup> <sub>-0.13</sub>	1.79 <sup>+0.10</sup> <sub>-0.04</sub>	1.76 <sup>+0.26</sup> <sub>-0.38</sub>
P7	2.96 <sup>+0.08</sup> <sub>-0.08</sub>	2.96 <sup>+0.10</sup> <sub>-0.09</sub>	0.94 <sup>+0.05</sup> <sub>-0.12</sub>	0.93 <sup>+0.13</sup> <sub>-0.12</sub>	1.78 <sup>+0.10</sup> <sub>-0.06</sub>	0.87 <sup>+0.90</sup> <sub>-0.03</sub>
P8	2.93 <sup>+0.07</sup> <sub>-0.06</sub>	2.88 <sup>+0.08</sup> <sub>-0.07</sub>	1.02 <sup>+0.14</sup> <sub>-0.06</sub>	1.01 <sup>+0.12</sup> <sub>-0.11</sub>	1.78 <sup>+0.07</sup> <sub>-0.04</sub>	1.40 <sup>+0.25</sup> <sub>-0.08</sub>

<sup>a</sup>Errors are 90% confidence level

<sup>b</sup>0.8–10.0 keV

<sup>c</sup> $\chi^2_\nu \sim 1.1$

<sup>d</sup> $N_H$  fixed at the Galactic value

<sup>e</sup>Global redshifts boosted up by 0.9%

TABLE 4  
SPECTRAL FITTINGS FOR P95<sup>a,b,c</sup>

Region	T(SIS0) <sup>d,e</sup> (keV)	T(SIS1) <sup>d</sup> (keV)	Abund (SIS0) (Solar)	Abund (SIS1) (Solar)	z (SIS0) (10 <sup>-2</sup> )	z (SIS1) (10 <sup>-2</sup> )
P0 <sub>FeL</sub>	2.84 <sup>+0.03</sup> <sub>-0.03</sub>	2.77 <sup>+0.03</sup> <sub>-0.07</sub>	1.46 <sup>+0.06</sup> <sub>-0.06</sub>	1.43 <sup>+0.07</sup> <sub>-0.08</sub>	2.71 <sup>+0.02</sup> <sub>-0.00</sub>	2.37 <sup>+0.04</sup> <sub>-0.07</sub>
P1 <sub>FeL</sub>	3.09 <sup>+0.09</sup> <sub>-0.09</sub>	2.86 <sup>+0.05</sup> <sub>-0.11</sub>	1.40 <sup>+0.15</sup> <sub>-0.16</sub>	1.34 <sup>+0.25</sup> <sub>-0.20</sub>	2.23 <sup>+0.47</sup> <sub>-0.19</sub>	2.35 <sup>+0.07</sup> <sub>-0.09</sub>
P2 <sub>FeL</sub>	3.24 <sup>+0.05</sup> <sub>-0.10</sub>	3.18 <sup>+0.10</sup> <sub>-0.09</sub>	1.19 <sup>+0.17</sup> <sub>-0.14</sub>	1.38 <sup>+0.20</sup> <sub>-0.18</sub>	1.63 <sup>+0.69</sup> <sub>-0.08</sub>	2.36 <sup>+0.06</sup> <sub>-0.06</sub>
P3 <sub>FeL</sub>	3.53 <sup>+0.11</sup> <sub>-0.12</sub>	3.82 <sup>+0.07</sup> <sub>-0.13</sub>	1.00 <sup>+0.17</sup> <sub>-0.13</sub>	1.55 <sup>+0.07</sup> <sub>-0.23</sub>	1.19 <sup>+0.67</sup> <sub>-0.07</sub>	2.32 <sup>+0.09</sup> <sub>-0.55</sub>
P4 <sub>FeL</sub>	3.70 <sup>+0.13</sup> <sub>-0.11</sub>	4.11 <sup>+0.17</sup> <sub>-0.16</sub>	1.13 <sup>+0.16</sup> <sub>-0.15</sub>	1.23 <sup>+0.28</sup> <sub>-0.18</sub>	1.71 <sup>+0.14</sup> <sub>-0.19</sub>	1.33 <sup>+0.34</sup> <sub>-0.50</sub>
P5 <sub>FeL</sub>	3.71 <sup>+0.14</sup> <sub>-0.14</sub>	3.99 <sup>+0.19</sup> <sub>-0.18</sub>	1.04 <sup>+0.20</sup> <sub>-0.16</sub>	1.09 <sup>+0.14</sup> <sub>-0.21</sub>	2.57 <sup>+0.82</sup> <sub>-0.40</sub>	1.37 <sup>+0.91</sup> <sub>-0.14</sub>
P6 <sub>FeL</sub>	3.59 <sup>+0.10</sup> <sub>-0.10</sub>	3.55 <sup>+0.12</sup> <sub>-0.19</sub>	1.29 <sup>+0.23</sup> <sub>-0.23</sub>	1.25 <sup>+0.25</sup> <sub>-0.26</sub>	3.60 <sup>+0.47</sup> <sub>-0.17</sub>	2.72 <sup>+0.18</sup> <sub>-0.98</sub>
P7 <sub>FeL</sub>	3.11 <sup>+0.14</sup> <sub>-0.12</sub>	3.23 <sup>+0.15</sup> <sub>-0.15</sub>	1.17 <sup>+0.24</sup> <sub>-0.17</sub>	1.34 <sup>+0.29</sup> <sub>-0.24</sub>	3.07 <sup>+0.54</sup> <sub>-0.51</sub>	2.54 <sup>+0.63</sup> <sub>-0.44</sub>
P8 <sub>FeL</sub>	3.13 <sup>+0.07</sup> <sub>-0.09</sub>	3.07 <sup>+0.13</sup> <sub>-0.11</sub>	1.45 <sup>+0.19</sup> <sub>-0.10</sub>	1.33 <sup>+0.27</sup> <sub>-0.18</sub>	2.63 <sup>+0.22</sup> <sub>-0.08</sub>	2.28 <sup>+0.09</sup> <sub>-0.48</sub>

<sup>a</sup>Errors are 90% confidence level

<sup>b</sup>FeK complex excluded (0.8-6 keV)

<sup>c</sup> $\chi^2_\nu \sim 1.1$

<sup>d</sup> $N_H$  fixed at the corresponding Galactic value

<sup>e</sup>Global redshifts boosted up by 1.2%

TABLE 5  
SPECTRAL FITTINGS FOR P93<sup>a,d</sup>

Region	Temp <sup>c</sup> (keV)	Abund <sup>c</sup> (Solar)	z <sup>b</sup> (10 <sup>-2</sup> )	$\chi^2_\nu$
P0	2.54 <sup>+0.07</sup> <sub>-0.04</sub>	1.02 <sup>+0.05</sup> <sub>-0.08</sub>	1.02 <sup>+0.02</sup> <sub>-0.02</sub>	1.19
P1	3.00 <sup>+0.17</sup> <sub>-0.14</sub>	0.98 <sup>+0.17</sup> <sub>-0.17</sub>	1.09 <sup>+0.15</sup> <sub>-0.15</sub>	1.125
P2	3.30 <sup>+0.14</sup> <sub>-0.15</sub>	0.91 <sup>+0.13</sup> <sub>-0.11</sub>	1.15 <sup>+0.44</sup> <sub>-0.06</sub>	1.132
P3	3.35 <sup>+0.16</sup> <sub>-0.15</sub>	0.81 <sup>+0.12</sup> <sub>-0.12</sub>	1.00 <sup>+0.03</sup> <sub>-0.07</sub>	0.994
P4	3.46 <sup>+0.20</sup> <sub>-0.20</sub>	0.87 <sup>+0.17</sup> <sub>-0.12</sub>	0.75 <sup>+0.27</sup> <sub>-0.28</sub>	1.095
P5	3.49 <sup>+0.26</sup> <sub>-0.24</sub>	0.75 <sup>+0.16</sup> <sub>-0.17</sub>	0.77 <sup>+0.79</sup> <sub>-0.21</sub>	1.013
P6	3.27 <sup>+0.17</sup> <sub>-0.16</sub>	0.71 <sup>+0.12</sup> <sub>-0.09</sub>	1.32 <sup>+0.27</sup> <sub>-0.22</sub>	0.995
P7	3.13 <sup>+0.13</sup> <sub>-0.13</sub>	0.74 <sup>+0.10</sup> <sub>-0.10</sub>	1.11 <sup>+0.31</sup> <sub>-0.15</sub>	1.055
P8	2.80 <sup>+0.20</sup> <sub>-0.16</sub>	0.85 <sup>+0.18</sup> <sub>-0.14</sub>	1.26 <sup>+0.76</sup> <sub>-0.06</sub>	1.399

<sup>a</sup> $N_H$  fixed at the Galactic value

<sup>b</sup>Errors are 68% confidence level

<sup>c</sup>Errors are 90% confidence level

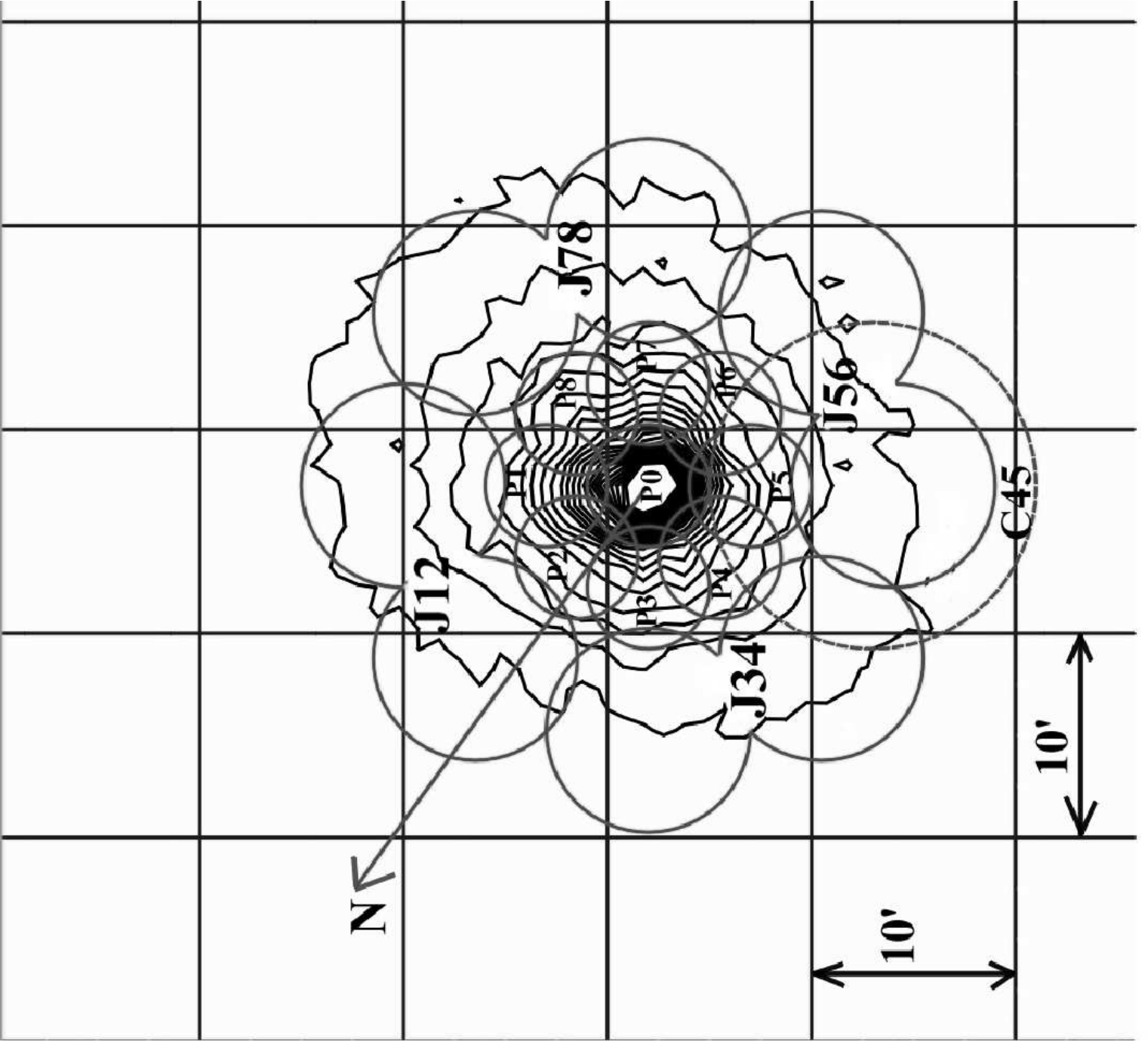
<sup>d</sup>Slope boosting correction for interchip gain differences

$$\begin{Bmatrix} S0C1 & S0C2 \\ S1C3 & S1C0 \end{Bmatrix} = \begin{Bmatrix} 1.01 & 1.012 \\ 1.006 & 1.01 \end{Bmatrix}$$

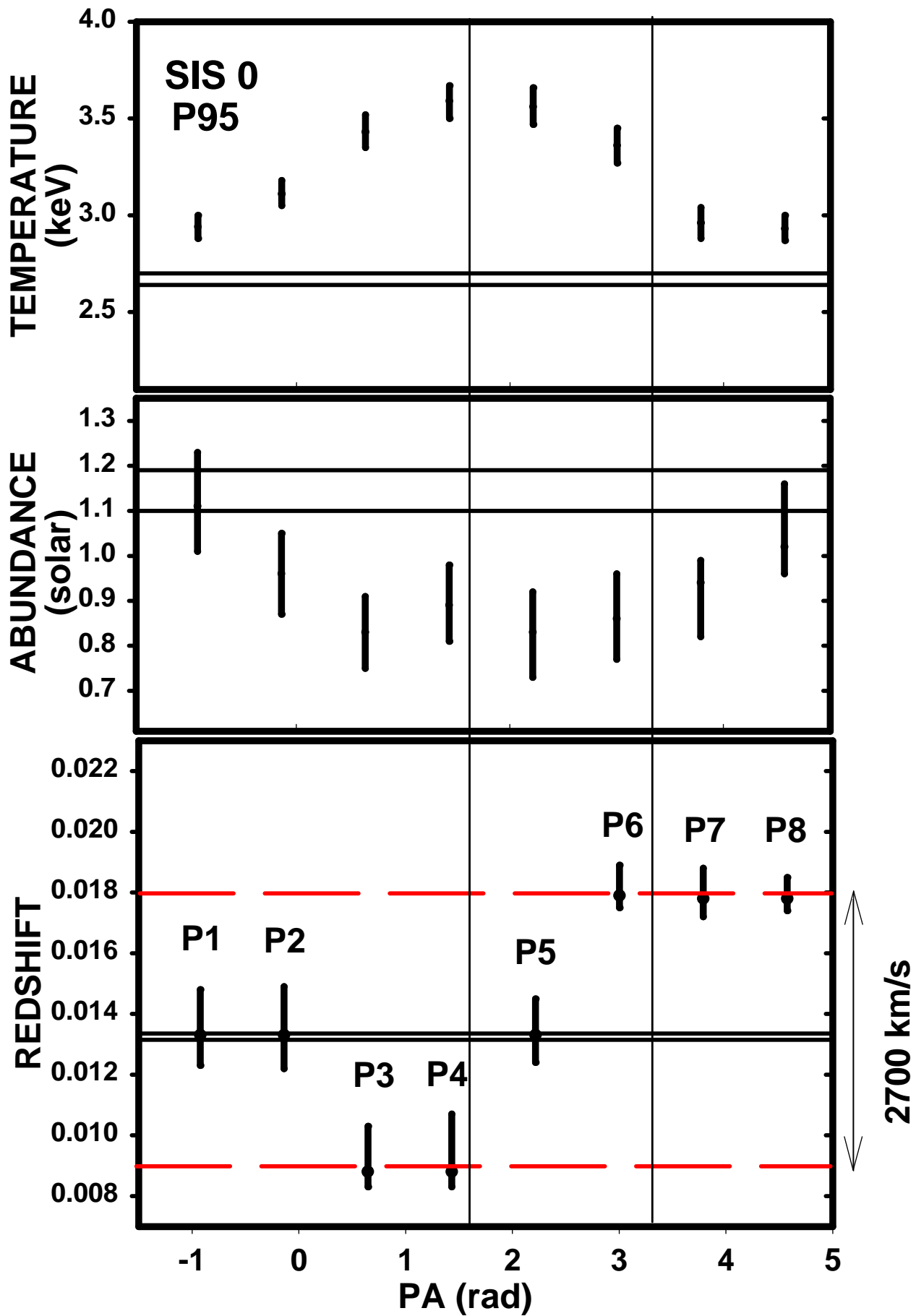
TABLE 6  
WEIGHTED AVERAGE VELOCITY DIFFERENCES FOR ALL POINTINGS <sup>a</sup>

Region	$\Delta V$ ( $10^3 \text{ km s}^{-1}$ )
P0	$0.07 \pm 0.45$
P1	$-0.06 \pm 0.52$
P2	$-0.63 \pm 0.47$
P3	$-1.84 \pm 0.45$
P4	$-2.04 \pm 0.54$
P5	$-0.36 \pm 0.74$
P6	$1.38 \pm 0.53$
P7	$0.71 \pm 0.61$
P8	$0.46 \pm 0.49$

<sup>a</sup> $1\sigma$  errors include spectral fitting as well as intrachip gain variations.

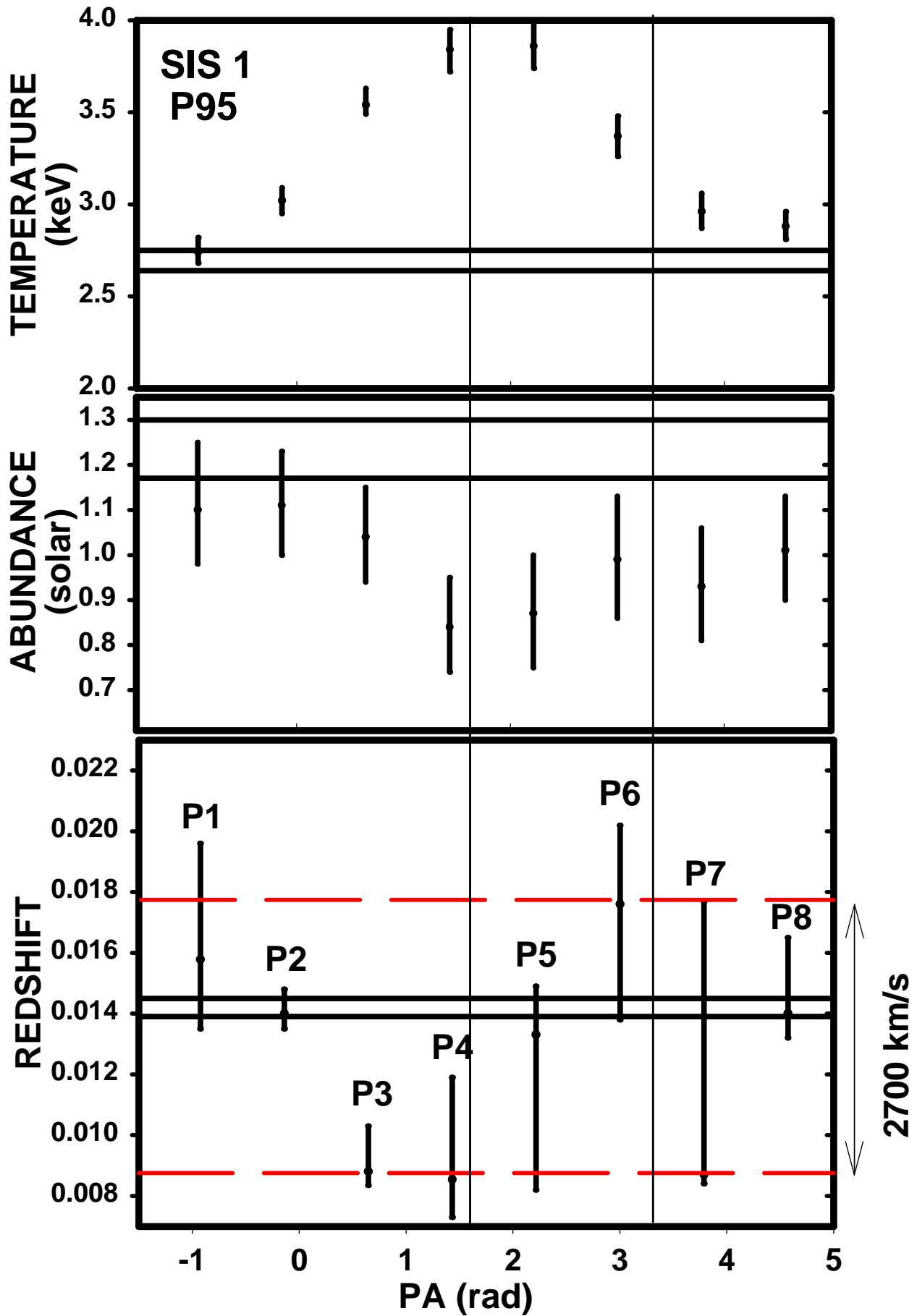






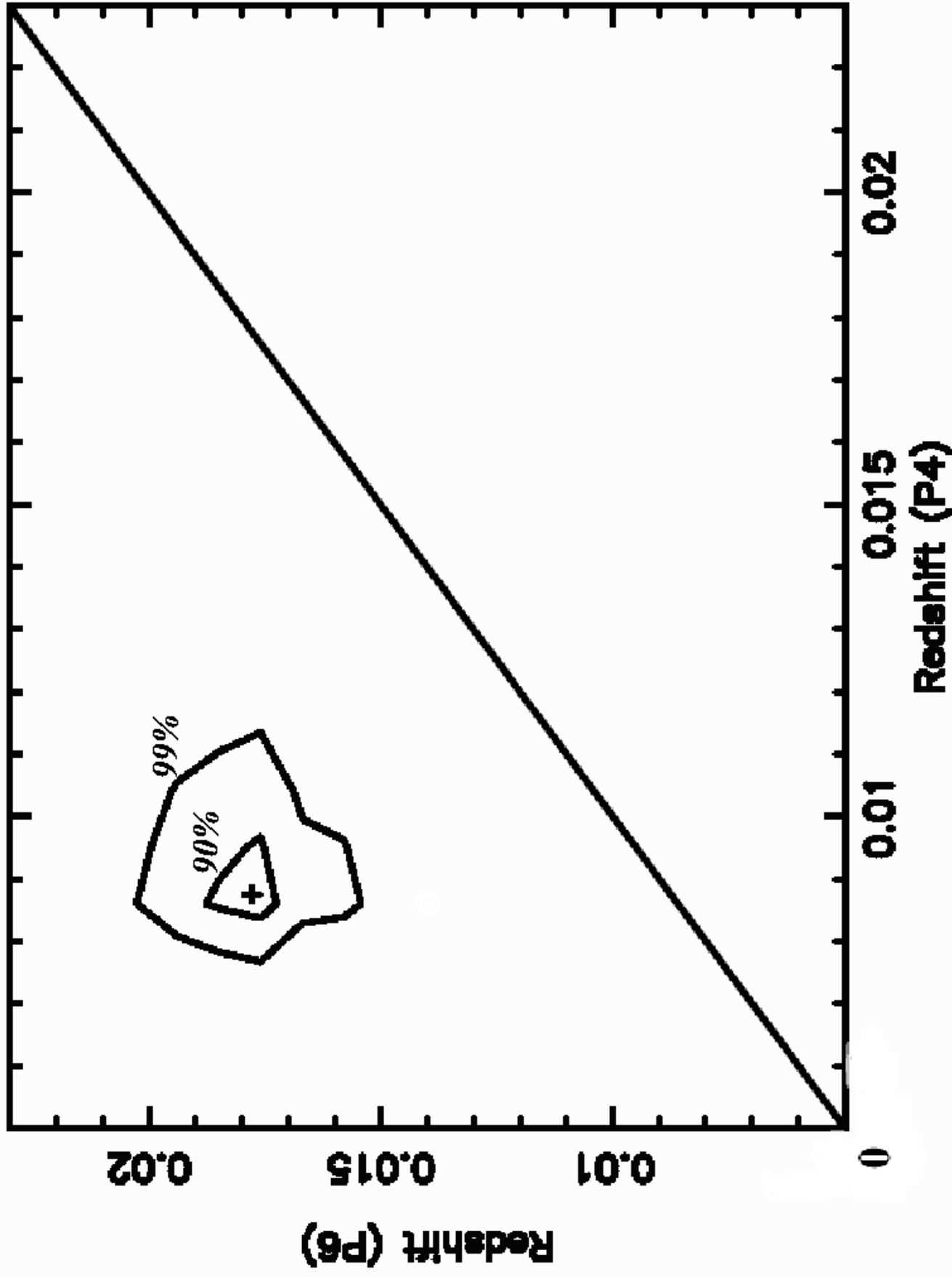




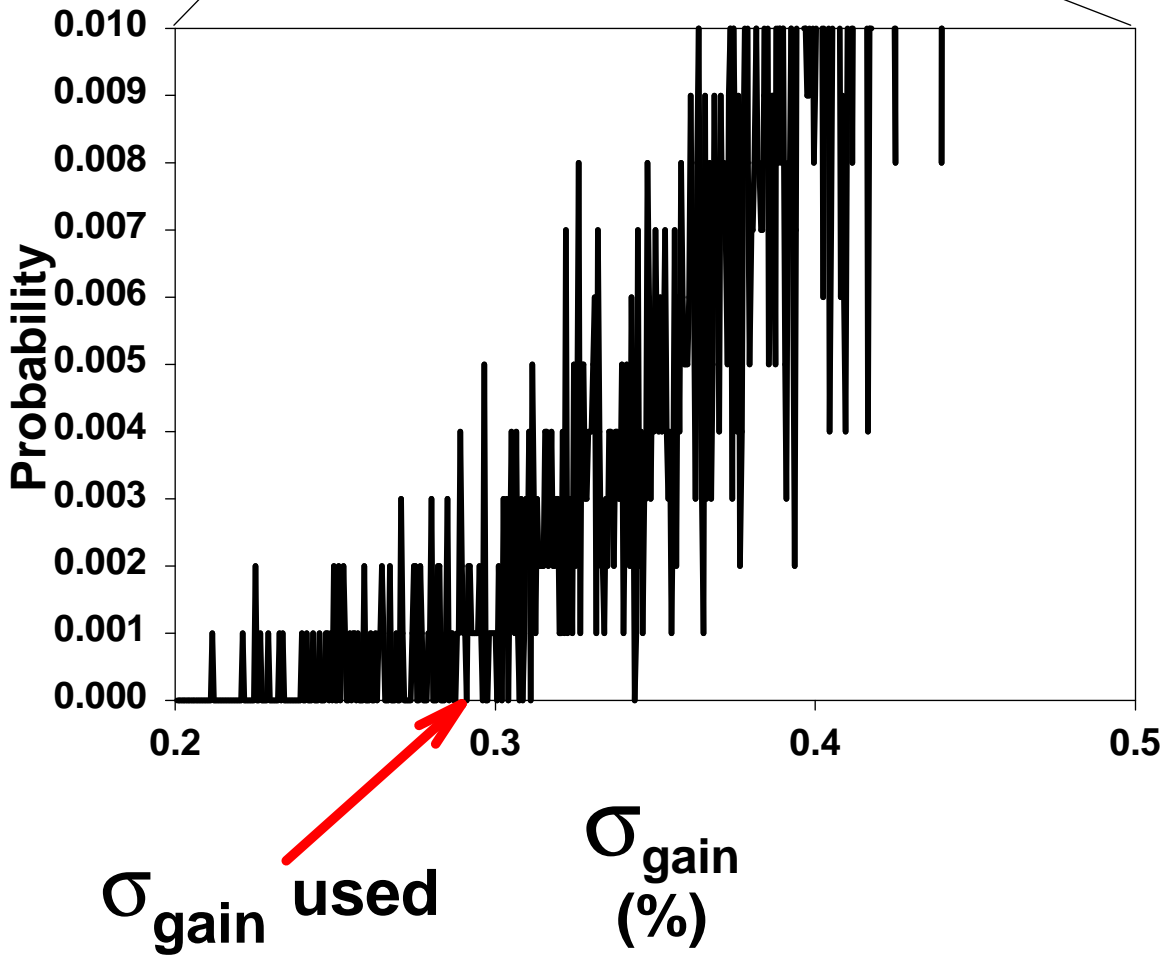
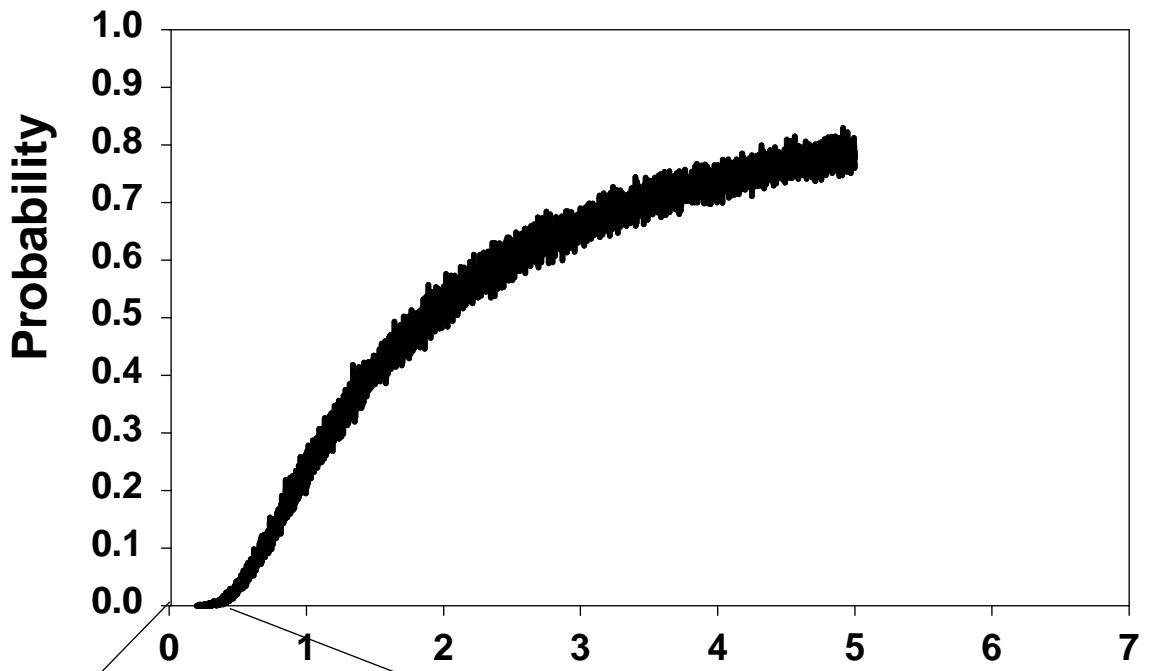




# CONFIDENCE CONTOURS

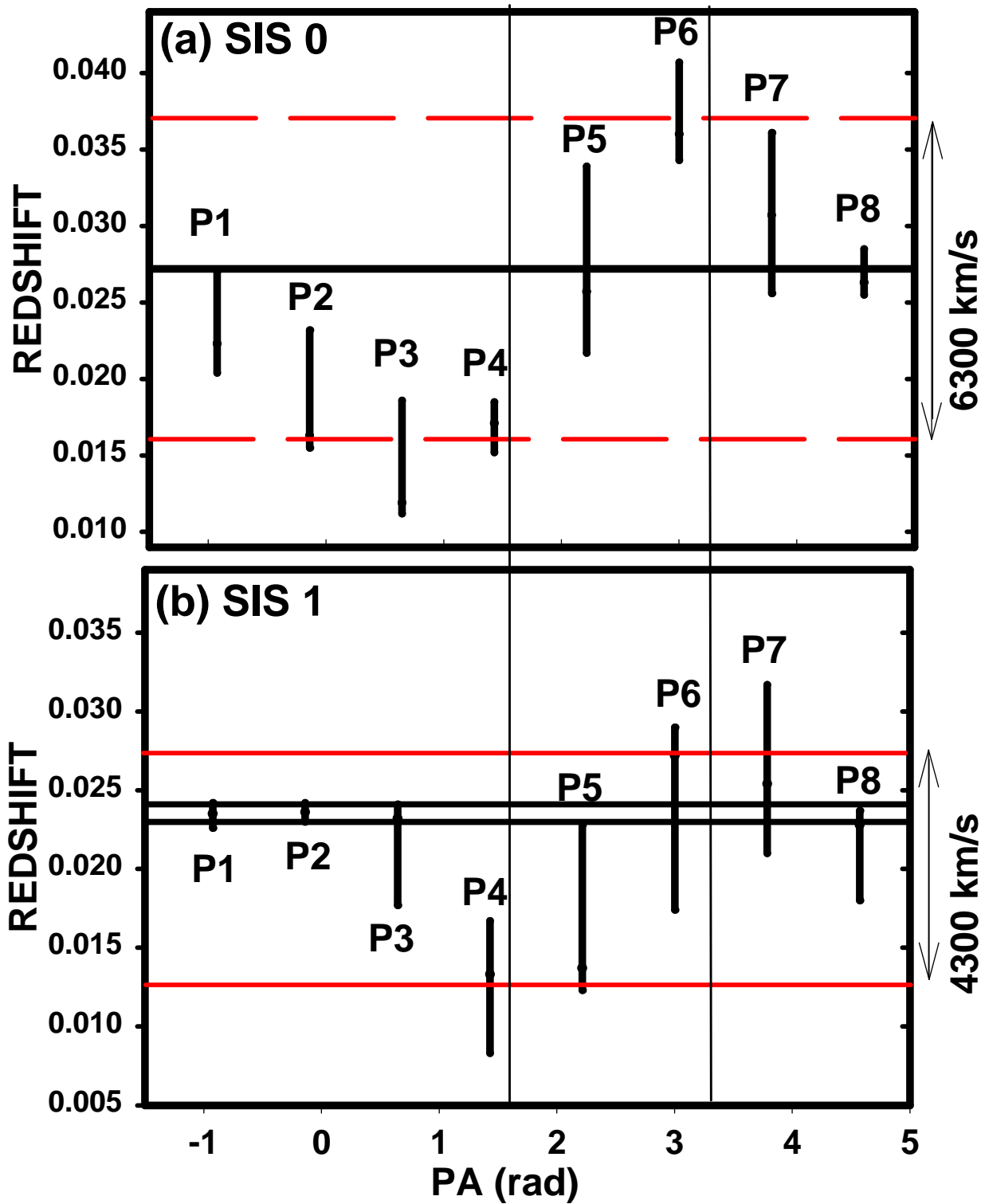






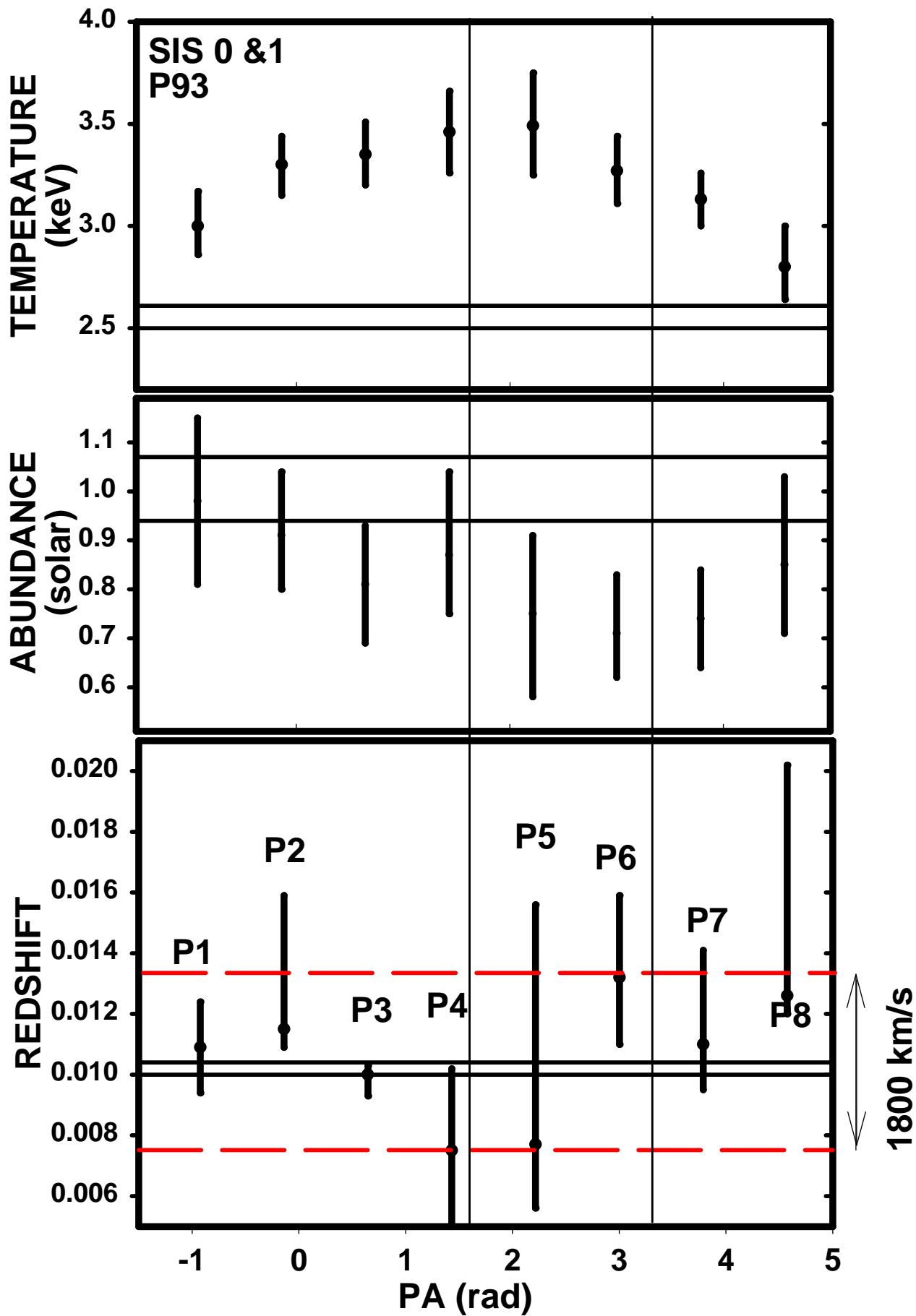


### P95 --- FeL











SIS 0&1  
P95 & P93

